NDT
Journal of Non-Destructive Testing

MDPI

Article

Design and Implementation of an SFCW Radar Platform for Environmental Monitoring

Jarne Van Mulders [1,*], Jaron Vandenbroucke [2], Merlin Mareschal [3], Bert Cox [1], Emma Tronquo [2,4], Hans-Peter Marshall [5], Sébastien Lambot [3], Hans Lievens [2] and Lieven De Strycker [1]

1 Department of Electrical Engineering, Katholieke Universiteit Leuven (KU Leuven), 9000 Ghent, Belgium; bert.cox@kuleuven.be (B.C.); lieven.destrycker@kuleuven.be (L.D.S.)
2 Department of Environment, Ghent University, 9000 Ghent, Belgium; jaron.vandenbroucke@ugent.be (J.V.); emma.tronquo@ugent.be (E.T.); hans.lievens@ugent.be (H.L.)
3 Environmental Sciences, Université Catholique de Louvain (UCLouvain), 1348 Louvain-la-Neuve, Belgium; merlin.mareschal@uclouvain.be (M.M.); sebastien.lambot@uclouvain.be (S.L.)
4 Department of Geoscience and Remote Sensing, Delft University of Technology (TU Delft), 2628 CN Delft, The Netherlands; e.tronquo@tudelft.nl
5 Department of Geosciences, Boise State University, Boise, ID 83725, USA; hpmarshall@boisestate.edu
* Correspondence: jarne.vanmulders@kuleuven.be

Abstract

Current satellite-based active microwave observations lack the temporal resolution needed to accurately capture rapid Earth system dynamics such as soil–plant–atmosphere interactions, rainfall interception, snowfall and rain-on-snow events. Ground-based radar systems can resolve these processes but typically rely on high-end VNAs, limiting their affordability and deployment scale. This work presents a low-cost SFCW radar system built around a compact, SDR-based VNA with an enhanced RF front end supported by remote-access firmware and a cloud-based back end with automatic backup. Calibration experiments and preliminary measurements demonstrate that the system achieves stable performance and is capable of capturing high-temporal-resolution microwave signatures relevant for climate monitoring.

Keywords: SFCW radar; L-band; C-band; calibration; sub-daily; tower-based; vegetation water content; soil moisture; snow

1. Introduction

Climate change monitoring relies heavily on satellite observations, complemented by ground-based and in situ measurement systems, to constrain model simulations. Active microwave remote sensing is increasingly used for observing ECVs [1–3]; however, many detailed Earth system processes remain unobserved due to temporal gaps in active microwave remote sensing data. For example, plants open their stomata during the day to capture atmospheric carbon at the expense of losing water through transpiration, redistributing moisture through the soil–plant–atmosphere continuum. While active microwave satellite observations (e.g., from Sentinel-1) are sensitive to such moisture variations, they can only provide a snapshot every 2 to 6 days (depending on the revisit time), and thus fail to observe these rapid changes. Other processes, like rainfall interception loss, dew formation or rain-on-snow events with subsequent changes in snow microstructure and stratigraphy, can at best only be captured by satellite observation at a single instant during the process evolution. The significance and delicacy of these processes for ecosystem functioning require ECVs to be monitored with great accuracy, yet their remote sensing is challenging,

Academic Editor: Fabio Tosti

Received: 2 December 2025
Revised: 15 January 2026
Accepted: 20 January 2026
Published: 1 February 2026

partly due to dynamic processes over short timescales, the microwave scattering impacts of which are poorly understood. Only a few studies have focused on sub-daily process variability [4–6], which is nowadays increasingly required by climate models. For instance, high-frequency process dynamics can be captured by ground-based microwave systems, as demonstrated by normal-incidence stepped-frequency continuous-wave (SFCW) radar monitoring of freeze–thaw cycles under snow cover [7] and by integrated hydrogeophysical inversion approaches coupling time-lapse ground-penetrating radar (GPR) data with hydrological modeling to retrieve soil water dynamics and hydraulic properties [8].

The growing need to capture these rapid dynamics in the water and carbon cycles has led to novel satellite mission concepts, such as SLAINTE [9], an ESA NEOMI. SLAINTE envisions a constellation of at least three monostatic L-band SAR satellites in Low Earth Orbit, providing observations spaced 6 h apart with a 3-day repeat cycle [10]. However, to truly demonstrate how missions like SLAINTE will close the observation gap, improved ground-based understanding of the microwave responses to sub-daily processes is critical. Airborne, spaceborne or UAV-based acquisition cannot (yet) obtain these measurement series with a high temporal resolution due to the limited overpasses, hardware restrictions and high costs. Recent drone-borne GPR studies have demonstrated strong potential for repeated time-lapse monitoring of root-zone soil moisture at multiday to seasonal scales in agricultural fields [11] and peatlands [12] but remain constrained by flight duration, regulations and operational costs, and therefore cannot deliver the continuous sub-daily sampling required for building process understanding. Therefore, the go-to solution to investigate dense time series of radar observations with high temporal resolution is tower-based systems. In the last two decades, several tower-based systems have been developed, including static polarimetric scatterometers to measure the radar cross-section of the area of interest [13–17], tomographic radar imaging systems relying on antenna arrays [18–21] and rail-mounted radars for repeated synthetic-aperture acquisitions [22–24]. Complementary fixed-position systems using ultra-wideband SFCW radar at normal incidence have also been employed to monitor temporal changes in soil and snow conditions [7,8,25].

Most of the aforementioned tower-based and rail-mounted systems rely on high-end VNAs to measure the backscatter signal, a methodology rooted in early developments of stepped-frequency full-wave radar modeling for GPR [26]. Cost-wise, such VNA-based systems strongly limit the number of sites that can be instrumented simultaneously within research projects such as WAVETRAX [27]. Other recent studies have explored compact and relatively low-cost VNAs in drone-borne GPR configurations for agricultural and peatland mapping and monitoring [11,12,28]. In particular, Wu et al. [11] and Henrion et al. [12] employed the gprSense® radar system [29], which integrates such a VNAs architecture with full-wave inversion to retrieve root-zone soil moisture. Nevertheless, professional-grade VNA-based systems are less suitable for large-scale and unattended deployment as they are constrained by their per-unit cost, power consumption and remote access. With recent developments in SDRs, a substantial part of the analog front end can now be replaced by embedded digital signal processing, enabling SFCW radar implementations based on an FPGA and a simplified RF front end. Furthermore, by shifting from specialized or proprietary electronics, as employed in previous experiments [17,30], to widely available commercial hardware, the risk of future incompatibilities or lack of technical support can be reduced, ensuring the long-term viability, scalability and adaptability of the system.

In this paper, we introduce a new SFCW radar sensor centered around **a low-cost SDR-based VNA**. These radar sensors are designed with measurement configurations that encompass those of several current, future and prospective spaceborne satellite missions in terms of operating frequencies, polarization combinations and incidence angle range. Furthermore, the sensors are deployed on tower infrastructure at research sites, where a

large number of in situ measurements are simultaneously collected with respect to soil, vegetation and snow properties. Therefore, (new) satellite geophysical retrieval methods can directly be tested using the dense time series of the tower-based radar observations and validated using the associated in situ measurements. Moreover, the unique combination of the radar and in situ data over a controlled footprint allows us to investigate how processes within the soil–vegetation–snow–atmosphere continuum impact radar measurements. These physical insights may help to further improve or extend the formulation of radiative transfer models.

Figure 1 provides an overview of the main steps, which are sub-divided into four phases. This manuscript primarily focuses on the research and development of the radar hardware and firmware, corresponding to Phase 1.

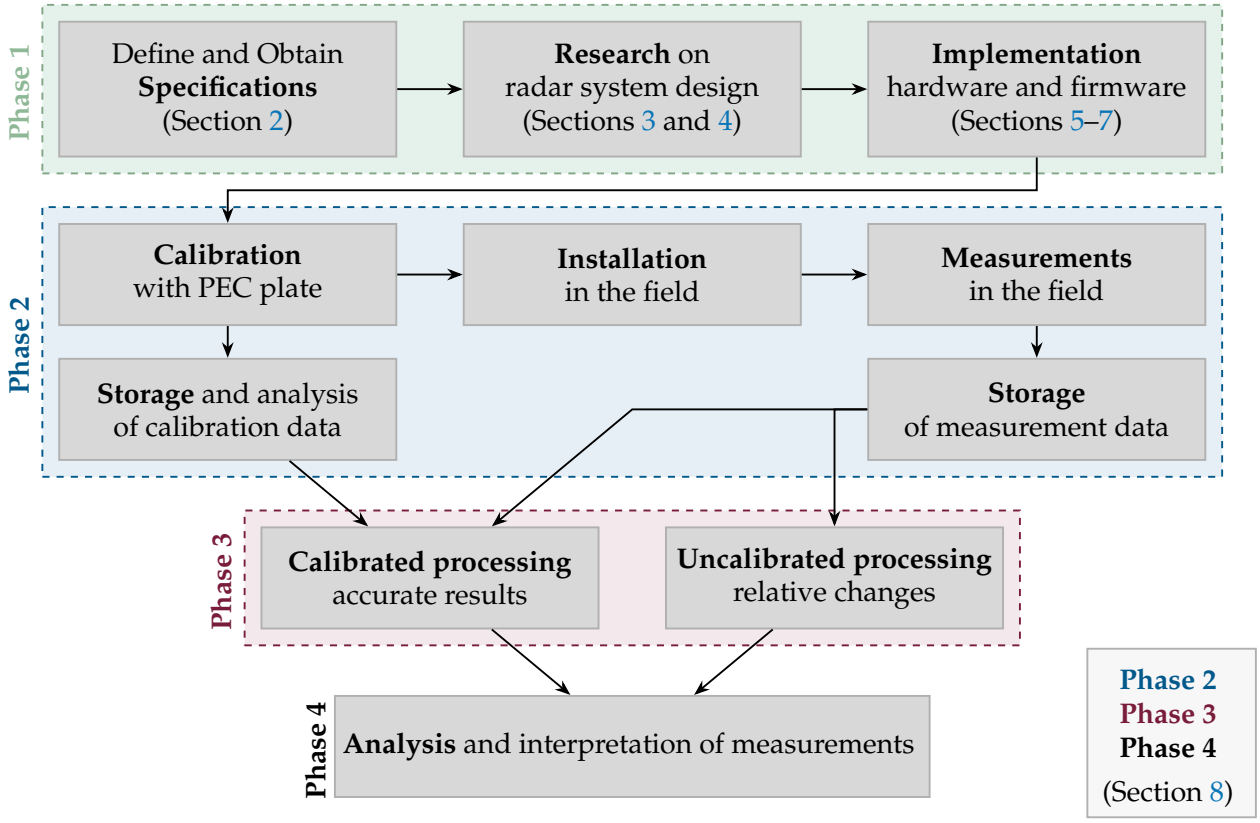

Figure 1. Steps in the research, design and deployment of the radar system.

The proposed static polarimetric scatterometer operates in both the L-band and the C-band and measures in two polarization planes (vertical–vertical, VV, and vertical–horizontal, VH). The setups, as shown in Figure 2, are secure in harsh weather conditions. They will operate alone in remote areas for periods of up to four years, with a network connection to control the operation and status and report the measured data. The primary objective of the developed hardware is to study the behavior of active microwave remote sensing observations in relation to surface processes and land–atmosphere interactions acting at the sub-daily timescale. It should be able to analyze the received data in both the frequency (e.g., understanding the microwave responses to sub-daily processes) and time (e.g., quasi-tomographic imaging of the snow–soil and vegetation–soil vertical profiles) domains. The main hypothesis is that an improved physical understanding of sub-daily processes and their impact on radar measurements offers an opportunity to improve upon the current state-of-the-art satellite retrievals of ECVs.

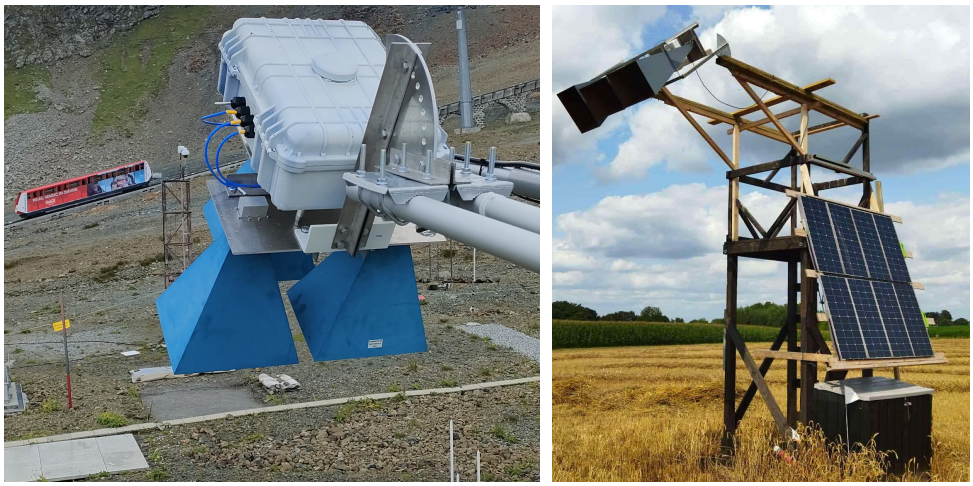

Figure 2. Field installation of the two radar systems showing two potential applications. The left tower, equipped with smaller horn antennas, operates in the C-band and is powered from the grid. The focus of this setup lies in measuring the soil–snow profile. This radar was installed during the summer at Weissfluhjoch, Switzerland, when the site was free of snow. The right tower, located in at Louvain-la-Neuve, Belgium, fitted with larger horn antennas, operates in the L-band and is supplied by a solar-powered battery system. Measurements performed at this location focus on the soil–vegetation profile.

In the remainder of this manuscript, we first outline the key challenges and technical requirements associated with the envisioned radar systems. Section 3 introduces the underlying radar technology and the chosen modulation scheme. Section 4 discusses the selection of the VNA and its role in enabling an SFCW radar architecture. The detailed hardware implementation is presented in Section 5, and the individual building blocks of the system are explored. Section 6 describes the firmware architecture and the back-end infrastructure that supports data acquisition, storage and visualization. To mitigate the risk of data loss, Section 7 provides an overview of the implemented backup strategies. Section 8 presents the calibration procedures and preliminary experimental results, corresponding to Phases 2, 3 and 4 in Figure 1. The focus of these first results lies in quasi-tomographic imaging of the snowpack. This section is followed by a discussion and outlook in Section 9. Finally, Section 10 summarizes the main conclusions of this work.

2. Challenges and Requirements

Radars are instruments that transmit radio waves and measure their reflections to determine, in most cases, the distance between the radar and an object. In this application, the aim is to investigate the amplitude and phase of the reflections from the soil, vegetation and snow throughout the soil–vegetation or soil–snow profile. Important technical requirements for the envisioned system are as follows:

1. The radar should be able to measure in the (lower) C-band and L-band to link the research to existing satellite missions such as Sentinel-1, the Radarsat constellation, the Advanced Land Observing Satellite-2 (ALOS-2), the Satellites for Observation and Communications (SAOCOM) and the NASA-ISRO Synthetic Aperture Radar (NISAR), as well as to mission concepts such as the Radar Observing System for Europe in L-Band (ROSE-L), Hydroterra and SLAINTE.
2. For measuring soil–snow and soil–vegetation vertical scattering profiles, a range resolution below 10 cm is sufficient.
3. The system should measure variables that evolve over timescales in the order of minutes. Therefore, a single measurement time must be in the order of seconds,

with frequent repeated measurements (every couple of minutes) over a long planned observation time (months/years).

This section focuses in more detail on the antenna selection, polarization and coupling aspects, the dynamic range of the radar, network requirements, performance and other key specifications and challenges associated with building a radar system that can be deployed and operated in the field.

Antenna beamwidth. The radar is intended to continuously monitor a specific area over periods ranging from several months to years. Its field of view is determined by the antenna beamwidth, which, together with the mounting height and installation angle, defines the radar footprint. To meet the application requirements, directive antennas with a 3 dB beamwidth below 20° are targeted. When installed at the default incidence angle of 40° (similar to satellite operations), this narrow beamwidth helps avoid strong specular reflections from the nadir. Furthermore, for the intended applications, such as tomographic imaging, the coverage area must remain small. Since the radar measures the average scattering contributions within its footprint, particularly at larger tilt angles, an overly wide footprint would blur the measurements and degrade interpretability [17].

Antenna polarization. Measurements of both co-polarization and cross-polarization are targeted, in line with satellite missions such as Sentinel-1, which operate in dual-polarization mode (VV and VH) over land, excluding polar regions. This furthermore allows polarimetric analyses, for instance, to investigate the extent of signal depolarization (from a V-polarized transmitted wave to an H-polarized reflected wave) following interactions with the snowpack, vegetation or soil. Signal depolarization mostly arises when the wave's polarization is altered due to scattering on (rough) anisotropic surfaces, multiple scattering or volume scattering. By acquiring both co-polarized and cross-polarized data, this effect can be quantified, enabling the computation of depolarization ratios (e.g., VV/VH), which are commonly used in, for instance, Sentinel-1 analyses of snow [31] and vegetation [32] properties. To achieve this, linearly polarized antennas are required. The polarization measurement depends on the mounting orientation of the antennas on the radar platform and the tilt angle of the radar. When the radar is installed at a certain angle, the alignment of the antennas relative to the ground becomes critical. To perform VV and VH measurements, a setup with one transmit antenna and two receive antennas is required. This means that a radar system with three linearly polarized antennas is needed to support both measurement setups.

Antenna bandwidth. The antenna bandwidth should match the operating frequency band to minimize reflections and ensure optimal radar performance. As both L- and C-band operation are envisioned, two antenna sets are required, each providing the appropriate bandwidth.

Antenna coupling. The coupling between the transmit and receive antennas should be minimized. Although the antennas, which are supposed to have very high directivity, are always pointed toward the illuminated area, some coupling can still occur. This coupling can be calibrated using open-sky measurements, as discussed further in Section 8.

Dynamic range of radar equipment. The received signals of interest in a radar system could span a broad range of signal strengths, so the receiver channels require a wide dynamic range. For instance, consider a C-band radar mounted on a 5 m high tower. When the signal travels to the ground and back, it covers a total distance of 10 m. Using the Friis transmission equation, the free-space path loss over this distance is approximately 66.4 dB at 5 GHz (lower C-band) assuming an ideal, lossless reflection from the surface. For the L-band (1–2 GHz), the corresponding free-space path loss ranges from approximately 52.4 dB to 58.5 dB. This represents a best-case scenario; in reality, losses are typically higher due to reflection losses, atmospheric effects and other factors. Some of this loss is mitigated by the high antenna gain. For example, a single antenna may provide a gain of around

20 dBi, and a combined transmit/receive antenna setup can exceed 40 dBi. Thus, antennas offering high gain are required in the implementation.

Network. The radar system requires a constant network connection, both to monitor its operational status and to continuously upload measurement data to a central server. This setup allows multiple research institutions to access the collected datasets from a shared central point. In addition, backup systems should be implemented, maintaining copies of all datasets stored on the central server to prevent data loss and ensure long-term reliability.

Robust standalone performance. The radar system must be capable of performing measurements continuously, 24/7, and should be able to automatically recover from power failures without manual intervention. The system must support a flexible temporal resolution, enabling sub-hourly measurement intervals and fully automated measurement cycles. Moreover, it should be able to operate for extended periods without human intervention while allowing key parameters to be easily and remotely configured.

Practical requirements. The radar system should be affordable, as multiple radar systems (up to five) will be actively collecting measurements over the same time period. Moreover, these should be temperature-monitored, as temperature variations can affect the behavior of electronic components and measurement stability. It is recommended to log the temperature inside and outside the enclosure, as well as near the RF front end and the edge computer, and store it together with the measurements, e.g., for potential calibration purposes. The radar will be mounted approximately 5 m above the ground on a tower. Mechanical strength is essential to ensure that the radar continuously monitors the same coverage area. The mechanical design should therefore be able to withstand harsh weather conditions and be fully waterproof. Furthermore, it is important that the monitored area remains free from disturbances caused by animals or humans, ensuring that only meteorological and environmental conditions influence the radar measurements.

3. Radar Technology and Modulation Scheme

The most common radar principles include pulsed radar, operating in the time domain, and CW radar, FMCW radar and SFCW radar, operating in the frequency domain.

3.1. Time-Domain Radar

In pulsed radar, a short pulse $s(t)$ is transmitted, and the reflection $r(t) = h(t) * s(t)$ is measured by directly sampling the echo of the transmitted pulse in the time domain (Figure 3). The relation between the two is given by the impulse response $h(t)$. In fact, $h(t)$ characterizes the reflections on the target area containing the required information. In GPR, pulse-based systems have been used for several decades in a wide range of applications, with [33] recently using it for surface-based GPR of glacial subsurface structures. In tower-based measurements, an example closely related to our application can be found in [17,30], where pulsed radars were used. This radar equipment was based on the XeThru X2 chipset [34]. It uses ultra-wideband (UWB) higher-order Gaussian approximation pulses with a bandwidth of about 2 GHz and centered around 5.4 GHz (the center frequency of the Sentinel-1 radar). For one measurement, the pulse is transmitted repeatedly, and the received responses are integrated to increase the SNR and extract functional information. A limitation is the occurrence of cross-talk artifacts at the beginning of the sampling process. Since these cross-talk signals are stronger than the reflected echoes, they impose a constraint on the maximum receiver gain achievable without damaging the radar. The X2 chipset is no longer available, and the new version, X4, uses another frequency band. To our knowledge, no other pulsed radar chipsets using the L- or C-band are currently commercially available at viable costs. Therefore, this time-based radar principle is not further investigated.

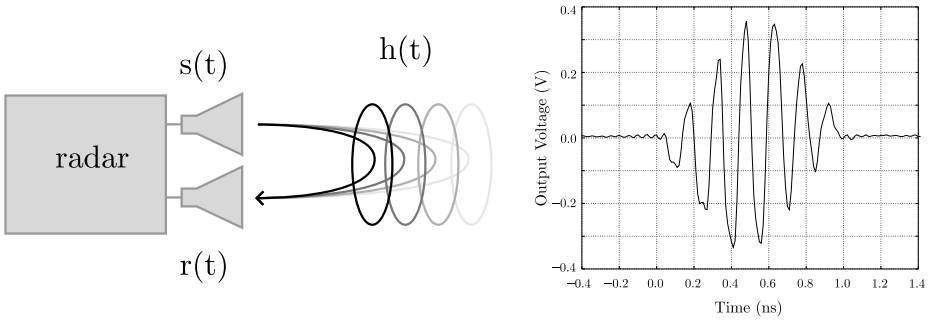

Figure 3. Low-complexity representation of a pulsed radar operating in the time domain (**left**) and an example of a Gaussian pulse transmitted by the XeThru X2 chipset with the PGSelect register set to 1 (**right**) [34].

3.2. Frequency-Domain Radars

The three other common radar principles make use of frequency-domain measurements to obtain information about the target. A CW radar transmits a constant-frequency signal and can be used for velocity measurements based on the Doppler radar principle. This principle is, for instance, commonly applied in the construction of speed camera systems. However, CW radar cannot be used for the purpose of this project, as it lacks the timing mark necessary to allow the system to accurately time the transmit and receive cycle and to convert this into range information. In other words, CW radars have no bandwidth by definition, and so range information cannot be obtained. FMCW and SFCW radars, on the other hand, are continuous-wave radar technologies that apply different frequency modulation schemes to enable range and, optionally, velocity measurements. The time–frequency progression of the transmitted signal is illustrated as a waterfall diagram in Figure 4. They both perform frequency sweeps. FMCW continuously sweeps the frequency in one single turn (e.g., with a chirp signal), whereas SFCW performs this sweep in several distinct single-frequency pulses, each at a different frequency. The range resolution is the minimal distance between targets at which they can still be distinguished separately by the radar system. The range resolution is an important characteristic for our application. The range resolution (ΔR) is inversely proportional to the bandwidth (β) of the sweep [35]:

$$\Delta R \propto \frac{1}{\beta} \tag{1}$$

Achieving a high range resolution requires a large effective bandwidth. In FMCW systems, this implies a wide instantaneous bandwidth capable of supporting the entire chirp. For the radar resolution targeted in this work (below 10 cm), such a broad, instantaneous bandwidth is difficult to realize using COTS low-cost hardware.

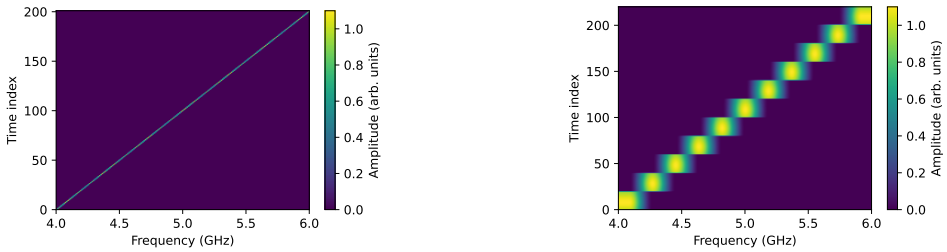

(**a**) Frequency modulated continuous wave. (**b**) Stepped frequency continuous wave.

Figure 4. Waterfall representation of the FMCW and SFCW radar principles, illustrating the evolution of the frequency sweep over time.

Stepped-frequency waveforms circumvent this limitation by synthesizing the required bandwidth across multiple pulses (of length τ_m), each transmitted at a constant carrier frequency, incremented by Δf for each subsequent pulse. As a result, the receiver only needs to accommodate the bandwidth of a single pulse of duration τ_m, which is approximately $\frac{1}{\tau_m}$. However, transmitting and receiving multiple frequency-stepped pulses increases the required dwell time required on the target to gather all necessary information, which is not an issue in our application as tower-based installations are static and the monitored ECVs vary very slowly.

Both FMCW and SFCW systems are well suited for identifying the characteristic spectral signatures of illuminated targets as they provide direct access to the frequency spectrum and, therefore, to relevant features. Nevertheless, as mentioned above, a time-domain representation is often required for studying the characteristic vertical scatter profiles of the target. Such a representation can be obtained by applying an IDFT to the frequency-domain data, a standard method in digital signal processing.

In our setup, we chose to implement the SFCW radars, as these are less demanding for hardware yet have similar performance capabilities to FMCW, making it a more cost-effective solution. The main disadvantage, the longer *time-on-target*, is mitigated by the fact that the ECVs we intend to measure are varying slowly, in the order of minutes rather than milliseconds, and the radar platform is not moving for tower-based applications. The longer measurement time is advantageous for the signal-to-noise ratio. Compared to pulsed radar systems, it is easy to flexibly increase or decrease the bandwidth of the signal (and, hence, the range resolution) so that, in practice, the actual main bandwidth limitation is in the antenna and other RF components. Additionally, a higher signal-to-noise ratio can be achieved, as SFCW systems have a higher average transmit power and a higher dynamic range [36] than pulsed radars. Another advantage over pulsed radars is the lack of ultra-fast sampling ADCs, or the use of inefficient sliding window digitizers [37].

3.3. Bandwidth and Range Resolution Considerations

As aforementioned, spectrally, our system wants to monitor microwave responses in the L-band and the lower C-band. At the same time, the time-domain representation for vertical scatter profile measurement is essential. For the latter, the range resolution is a crucial parameter. In this sub-section, the range resolution of the targeted SFCW is considered.

The range resolution ΔR can be calculated from the FWHM time τ of the (equivalent) time pulse used by the radar:

$$\Delta R = \frac{c\,\tau}{2} \tag{2}$$

where c is the phase velocity in the considered medium, which is assumed to be approximately 3×10^8 m/s, as the medium is mainly air in our case. The factor $1/2$ is compensating for the fact that the signal travels back and forth in this monostatic radar configuration.

An SFCW radar measures the transfer function $H(f)$ at discrete frequencies f_k by transmitting an unmodulated carrier at that frequency and then registering the phase difference and the amplitude ratio between the transmitted and received signal. The (time-domain) impulse response $h(t)$ is then calculated using the IDFT.

An SFCW radar typically uses a rectangular window in the frequency domain during the measurements, as shown in Figure 5. This rectangular frequency window results in a sinc-shaped pulse in the time domain when the IDFT is applied. Other windows, trading-off the width of the main lobe and the height of the side lobes of the time-domain pulse, can be applied in postprocessing, if useful for the application. The impact of such windowing on the range resolution must be taken into account. The relation between the SFCW bandwidth β and the FWHM of the sinc's main lobe τ_{sinc} is

$$\tau_{sinc} = \frac{1}{\beta} \tag{3}$$

With Equations (1) and (3), the range resolution can be linked to the bandwidth of the SFCW radar. A minimum bandwidth of 1.5 GHz is needed to fulfill the requirement of a range resolution better than 10 cm. For example, in the lower C-band, a bandwidth $\beta = 2$ GHz is considered in our system. This results in a range resolution $\Delta R = 0.075$ m.

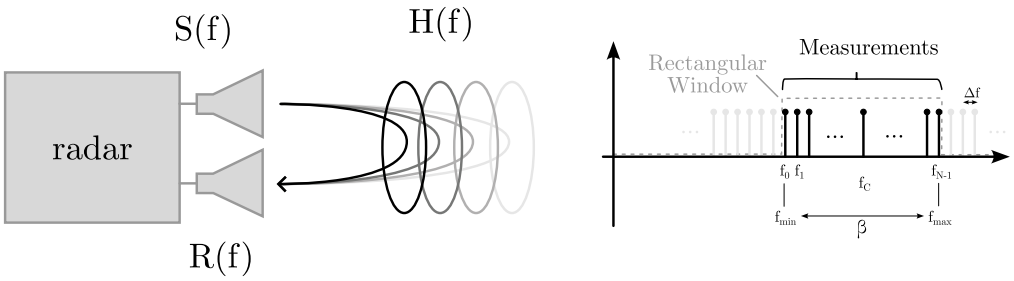

Figure 5. Stepped-frequency continuous-wave (SFCW) radar system, where several consecutively unmodulated carriers at different frequencies are transmitted. The bandwidth (β) depends on the set minimum and maximum frequencies, set by a (square) filter. The frequency step is defined by Δf.

With an SFCW radar based on a VNA, the bandwidth can be flexibly adapted by changing the measurement range of the VNA. Higher bandwidths would result in better range resolutions, but there are some caveats. Firstly, when increasing the bandwidth, other RF components such as LNAs, PAs, switches and antennas should be selected accordingly. Secondly, we are interested in the target's response in a certain frequency band; increasing the bandwidth implies a broader spectral measurement. Satellite observations typically use a small bandwidth combined with SAR processing to achieve a good range resolution [9]. To transfer scientific insights from tower-based observations to satellite observations, the bandwidth should not be overly large. On the other hand, using a small bandwidth to conform more to satellite applications would require an antenna array or a movable antenna to achieve a good range resolution. This would make the system far more expensive and less robust when deployed in remote areas with harsh weather conditions.

It is informative to compare with the earlier C-band tower-based snow measurement campaigns from [30] using a pulsed radar based on the XeThru X2 chipset, as they proved to have an adequate range resolution and are a good reference for our application.

The pulsed radar system uses an approximation of a Gaussian pulse. The Gaussian pulse duration can be deduced from the left-hand side of Figure 6 [34]. The FWHM of this pulse is about $\tau_{Gauss} \approx 0.5$ ns. Hence, using Equation (2), the range resolution can be calculated from the FWHM:

$$\Delta R_{Gauss} = \frac{c\ \tau_{Gauss}}{2} = 0.075\,\text{m} \tag{4}$$

Using a 2 GHz bandwidth in the SFCW system will give a comparable range resolution. For comparison with the SFCW radar system, it is also informative to see what bandwidth is used by this pulsed radar system. For a Gaussian pulse, the product of the -6 dB bandwidth $\beta_{-6dB,Gauss}$ and the FWHM τ_{Gauss} is 0.883.

$$\beta_{-6dB,Gauss} \cdot \tau_{Gauss} = 0.883 \tag{5}$$

Therefore, $\beta_{-6dB,Gauss} \approx 0.883/0.5\,10^{-9}\,\text{s} = 1.76$ GHz. This is consistent with the -10 dB bandwidth of $\beta_{-10dB,Gauss} = 1.8$ GHz stated in the datasheet (see also Figure 6).

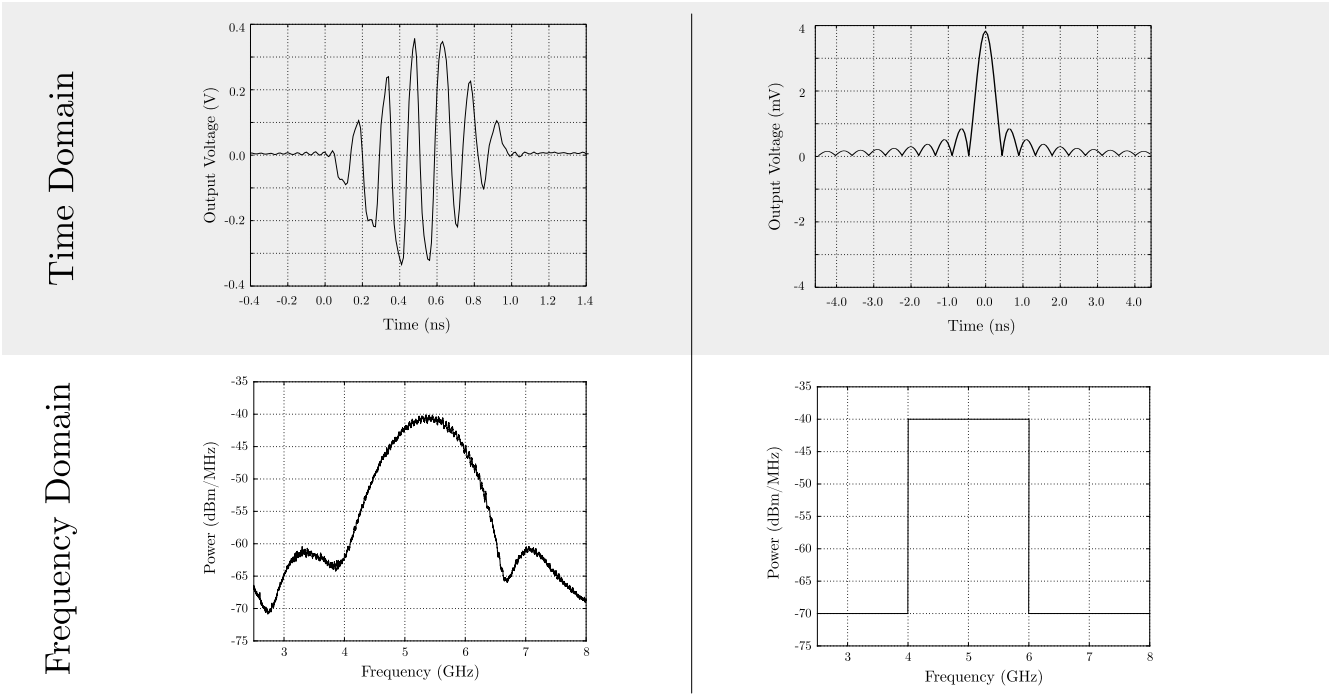

Figure 6. The higher-order Gaussian pulse signal and corresponding bandwidth of the XeThru X2 chip [34] (**left**) and an SFCW with a bandwidth of 2 GHz and center frequency of 5 GHz and the corresponding sinc function (**right**).

The inverse Fourier transform of the frequency measurements is performed in a discrete way (IDFT). Therefore, the maximum range the SFCW radar can cover is limited; otherwise, spatial aliasing occurs. The maximum range R_{max} depends on the frequency step Δf.

$$R_{max} = \frac{1}{\Delta f} \frac{c}{2} \tag{6}$$

Given a certain bandwidth β, $\Delta f = \frac{\beta}{N}$, with N being the number of frequency measurements (see Figure 5), and so the number of measurements N must be high enough to avoid spatial aliasing. Since, with tower measurements, the maximum distance is limited to a few meters, in practice, this is not a real limitation in the system. For example, with a bandwidth of $\beta = 2$ GHz and $N = 256$ measurements points, the maximum range (R_{max}) is about

$$R_{max} = \frac{N}{\beta} \frac{c}{2} = \frac{256 \cdot 3.10^8}{2.10^9 \cdot 2} = 19.2\,\text{m} \tag{7}$$

This is larger than the 7.78 m direct range when the radar is positioned at 5 m under an incidence angle of 40°. However, the IDFT's processing gain increases with an increasing number of points N, so, in noisy environments, it is better to use a higher number of measurements [38].

Note that interpolation in the time-domain signal is mathematically performed by padding the measurement data with zeroes for frequencies above f_{max} before performing the IDFT.

4. VNA Selection

By design, a VNA generates an SFCW spectrum, as it adjusts the frequency in discrete steps. The selection of an appropriate VNA constitutes a critical aspect of the radar implementation approach adopted in this study. Typically, these instruments are associated with a very high cost. However, recently, new low-cost models have been introduced to the

market, such as the LibreVNA, NanoVNA and LiteVNA. Table 1 presents a comparison between the LibreVNA and a high-end counterpart, detailing their key specifications.

Table 1. Overview of the key specifications of two VNA models.

VNA	Max Freq.	RF Power	Dynamic Range	Points	DC Power	Phase Noise	IFBW	Price
LibreVNA [39]	6 GHz	0 dBm	>50 dB	4501	6–7 W	−103 dBc/Hz	10 Hz	≈700 EUR
PicoVNA 108 [40]	8.5 GHz	6 dBm	≤124 dB	10,001	<25 W	−90 dBc/Hz	10 Hz	≈11K EUR

The frequency range of the PicoVNA covers the entire C-band, whereas the LibreVNA is limited to 6 GHz. This is sufficient because we target the lower C-band. Data captured with the LibreVNA can be quantitatively compared with Sentinel-1 data, as the 5.4 GHz center frequency of the Sentinel-1 radar is lower than this maximum frequency of 6 GHz. Although the output power of the LibreVNA is limited, this limitation can be mitigated by integrating additional PAs. Moreover, the inclusion of these amplifiers also increases the effective dynamic range of the measurement system, at the cost of possibly more noise. The dynamic range of the LibreVNA for S21 measurements is 60 dB, compared to only 55 dB for S12 measurements at frequencies above 2940 MHz. Consequently, S21 measurements were consistently selected for use in these radar systems [41]. In contrast, the PicoVNA provides a substantially higher dynamic range according to its specifications. Furthermore, this latter VNA supports hardware that enables a significantly larger number of points per sweep compared to the LibreVNA. However, in the current radar systems, fewer than 1000 points per sweep is appropriate, making the specifications of the LibreVNA sufficient for this application.

The power consumption of the LibreVNA is low compared to other VNA models, ranging from only a few Watts in standby to approximately 6–7 W during a sweep. This low power consumption makes the device particularly suitable for solar- and battery-powered deployments.

Finally, the phase noise is listed in Table 1 for both instruments at a 10 kHz offset from the carrier: the LibreVNA and the PicoVNA operating below 1 GHz. Phase noise by itself does not necessarily pose a major issue for radar performance. If the impact of phase noise or other noise sources on the radar performance is well understood, an appropriate SRI for an SFCW radar can be selected. Range uncertainty is the focus rather than velocity uncertainty, since only static measurements are performed with the radar systems proposed here. According to [42], the range (R) uncertainty σ_R [m] in an SFCW radar is given by

$$\sigma_{R_{max}} \propto \frac{R \cdot f_{max}^{0.5} \cdot \sigma_T}{\sqrt{SRI}}, \tag{8}$$

with σ_T [s] being the RMS jitter from the internal signal generator, f_{max} [Hz] the maximum sweep frequency and SRI [s] the stepped repetition interval. RMS jitter indicates that the internal reference clock is not ideal. Small random timing deviations of the signal edges lead to a broadening of the signal spectrum, which manifests as a wider frequency peak. The single-sideband (SSB) phase noise of the DSB221SDN (0.5 ppm) oscillator used in the LibreVNA is −135 dBc/Hz (offset 1 kHz) and is degraded by the subsequent components in the signal chain to the value listed in Table 1. As mentioned earlier, a VNA has been selected for the proposed SFCW radar system. However, this principle can also be implemented using an SDR, as suggested in [43,44]. In an SDR radar system, the SRI can be explicitly selected, whereas this is not possible on a VNA. It can only be adjusted indirectly by setting a low IFBW and/or increasing the averaging, which determines the duration of each frequency step. Selecting a low IFBW increases the number of time-domain samples

per frequency point, which extends the dwell time at each step and indirectly improves the effective SRI. When averaging is enabled on the VNA, two types can be distinguished: point averaging and trace averaging. Point averaging repeats measurements at each frequency, effectively increasing the dwell time, whereas trace averaging repeats entire sweeps and averages multiple measurements per frequency point. According to the datasheet, the LibreVNA supports averaging, which is implemented as a moving average across multiple sweeps. This indicates that the software provides trace averaging [39].

A VNA is typically calibrated to measure only the imperfections of the DUT, excluding additional losses from cables, RF switches, connectors or reflections due to impedance mismatches. Standard calibration uses a kit (open, short, load, through) to remove these systematic errors. In the radar setup presented here, however, the VNA is calibrated by positioning the radar in front of a reflecting plane, as described in Section 8, accounting for system-level reflections, cable losses and amplifier gains.

5. Radar Hardware Implementation

Figure 7 presents the internal architecture of **the new low-cost SDR-based VNA radar system** in a block diagram representation. The PSU and DC/DC converters provide 5 V and 12 V of power, either from a grid-connected mains supply (e.g., the C-band radar deployed in Davos, Switzerland) or from an off-grid external energy storage system with solar panels delivering the same mains voltage (e.g., the L-band setup in Louvain-la-Neuve, Belgium, depicted on the right side of Figure 2). Network connectivity is provided via a modem, and the Raspberry Pi 5 or edge computer manages the entire system. The operating system runs from an SSD to ensure additional stability and sufficient backup data storage. The 40-pin connector is used to interface with a custom HAT, responsible for supplying power and controlling the radar's various peripheral devices. The HAT supports two connectors (TMP1, TMP2) to monitor the temperature inside and outside the flight case. Furthermore, an SMA connector is available to control the RF switch. An integrated RTC ensures correct timestamps after a power cycle, even if the network connection is not immediately available. By combining a small additional battery with the RTC on the HAT, the Raspberry Pi can maintain the correct time across power cycles. The edge computer is connected via USB to the LibreVNA. A LibreVNA service runs on the system, ensuring that the LibreVNA software application (release 1.6.2), with an optional GUI, is operational. In addition, this application provides a network interface over TCP/IP sockets, allowing remote access and control of the VNA. This allows commands and queries to be sent from a Python (release 3.11.2) script running on the same system to the LibreVNA application, while the GUI can be disabled.

As previously outlined, directional antennas with a narrow beamwidth are required and could, for example, be patch antennas, parabolic reflector antennas or horn antennas. In these radar setups, the latter are specifically chosen because their typical beamwidth matches the required value of less than 20° ($HPBW_{ant} = 17.5°$). Furthermore, the measurement procedure requires both VV and VH polarimetric observations. In a strict sense, this would necessitate the use of a four-port VNA, of which three ports would be utilized. However, given the static nature of the measurements, it is not essential to acquire the co- and cross-polarization channels simultaneously. Consequently, an RF switch may be incorporated on the receiver side, enabling the use of a conventional two-port VNA. The RF front end is therefore simplified to two VNA ports. Port P1 is directly connected to horn antenna 1. Port P2 is connected to a two-way RF splitter whose two output ports are each connected to a horn antenna. As discussed in Section 4, the dynamic range of the LibreVNA is inherently limited compared to higher-end instruments. By augmenting the front end with a PA and LNA, this limitation can be mitigated. The power amplifier

(ZJL-7G+) provides about 10 dB of gain and the LNA (ZX60-83LN-S+) adds 20 dB, resulting in roughly 30 dB of total gain, excluding cable losses. The five RF cables (FL141-24SM+), each introducing up to 0.9 dB of attenuation, contribute a worst-case loss of 4.5 dB, yielding a net gain of approximately 25.5 dB. This additional gain improves the radar link budget and the effective detectability of weak targets. While the inclusion of the PA and LNA introduces some SNR degradation due to their respective noise figures, this effect remains limited, as the noise figures of the LNA (1–2 dB) and PA (5–6 dB) only moderately raise the overall receiver noise floor. Moreover, the transmitted signal generated by the VNA exhibits a high intrinsic SNR.

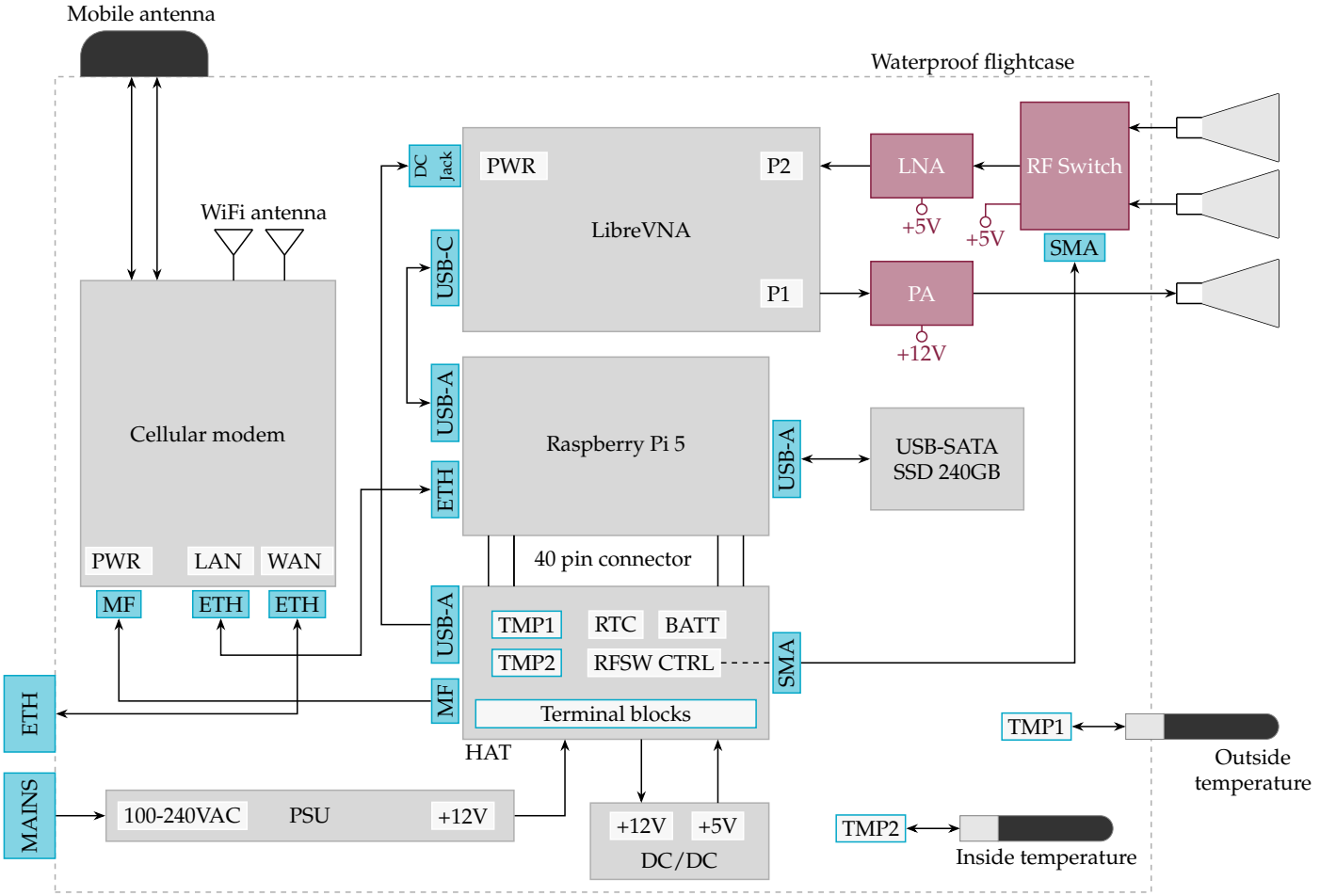

Figure 7. Representation of the L- and C-band SFCW radar setup. All RF cables connecting the VNA, LNA, PA, RF switch and horn antenna are high-quality 18 GHz 50 Ω coaxial cables with SMA connectors. TMP stands for temperature connector, ETH for Ethernet connector, RFSW for RF switch and MF for Micro-Fit connector.

The mechanical construction of both radar systems is illustrated in Figure 8 and consists of identical hardware in both cases, except for the horn antennas and the metal framework.

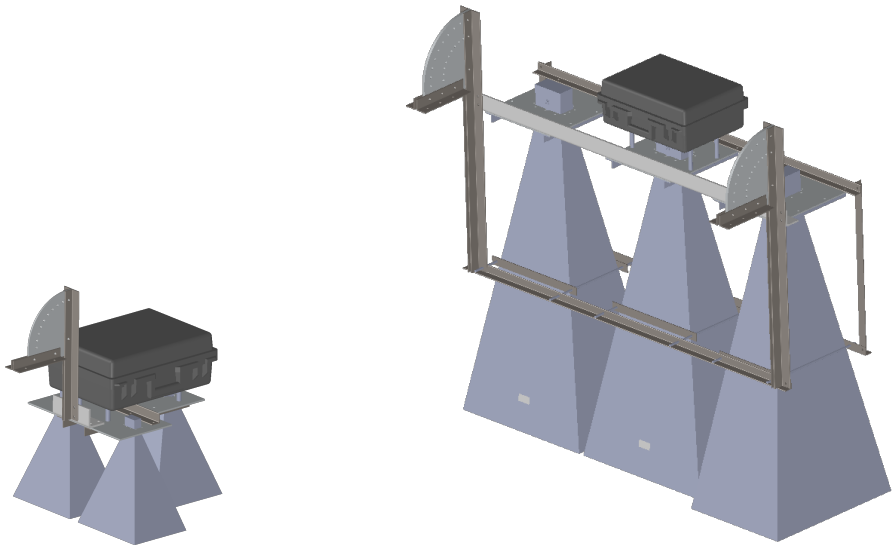

(a) (b)

Figure 8. Radar designs. The black flight case contains the electronic components. Both radars contain aluminum tilt plates for adjusting the incidence angle of the horn antennas. (**a**) C-band radar assembly designed to mount three PEWAN187-20SF horn antennas. (**b**) L-band radar assembly designed to mount three PEWAN430-20SF horn antennas.

6. Firmware and Back-End Infrastructure

In addition to the previously mentioned LibreVNA application service in Section 5, two other services run on the radars: a scheduler script and a Flask-based API service. The scheduler is responsible for performing periodic VNA measurements and polling the radar's system sensors. A web-based API service provides an interface that allows users to adjust the VNA configuration through a graphical interface.

The VNA results obtained after a VNA sweep are transmitted to a central server running an InfluxDB system. In addition, a Grafana instance is hosted on the same server to facilitate monitoring of the radar systems and visualize the collected data. The services running on the central server, such as InfluxDB and Grafana, are securely linked to a domain name through Cloudflare. Using a write API key generated in InfluxDB, the radars can transmit data to the server in a secure manner.

In this work, three types of InfluxDB data packets, hereafter referred to as frames, are defined as structured sets of tags, fields and a timestamp that are transmitted to the central server. The VNA data are transferred according to the structure shown in Table 2. The timestamp is defined as the *time* field, while the radar name, polarization and frequency are used as *tags*. The actual measurement data, included as *fields*, consist of a complex value expressed in Cartesian form. Each combination of tags must be unique for a given timestamp. Otherwise, the corresponding data in InfluxDB will be overwritten. Consequently, the frequency also has to be defined as a tag.

Table 2. Structure of the frame used to transmit radar measurements, consisting of complex values for each frequency point of the SFCW implementation.

Timestamp	Radar	Polarization [VV or VH]	Frequency [Hz]	Re [-]	Im [-]
.time()	.tag()	.tag()	.tag()	.field()	.field()

The second frame is used to periodically transmit system information from the radar, such as CPU load, CPU temperature, VNA temperature and indoor and outdoor temperature. This frame is shown in Table 3.

Table 3. Structure of the frame used to transmit radar system measurements.

Timestamp	Radar	CPU [%]	Disk [%]	CPU [°C]	VNA [°C]	Inside [°C]	Outside [°C]
.time()	.tag()	.field()	.field()	.field()	.field()	.field()	.field()

The final frame is used to transmit the VNA settings. A transmission occurs only when the settings are modified through the web server hosted on the Raspberry Pi. This allows the current configuration, including the measured S-parameter, center frequency, frequency span, number of points, IFBW and VNA output power level, to be immediately viewed on the Grafana dashboard. The structure of this frame is presented in Table 4.

Table 4. Structure of the frame used to store the most recently configured VNA settings.

Timestamp	Radar	S-Parameter	Center [Hz]	Span [Hz]	Points [-]	IFBW [Hz]	Power [dBm]
.time()	.tag()	.field()	.field()	.field()	.field()	.field()	.field()

On the web page hosted by the Raspberry Pi of the radar, the time intervals for radar measurements and for polling the system sensors can be configured individually. In addition, users can choose between single measurements, for example, for calibration, or automatic measurements to perform periodic measurements in the field. The Python code can be found in the GitHub repository [45].

7. Backup Implementations

Ensuring continuous data acquisition with minimal dead zones is essential to enable reliable postprocessing of the measurements. To meet this requirement, several supporting mechanisms were evaluated and implemented. However, the current design does not incorporate any form of power backup, making data loss the primary risk. Under the assumption that a stable 120 VAC or 230 VAC power supply is consistently available, the following backup mechanisms are provided:

A **wide-area network (WAN) connection** can be established in several ways. Once this link is available, it becomes possible to send data to the central server, monitor the radar and manage it remotely. In practice, the system first attempts to use (1) a WAN Ethernet connection, as it provides the most reliable and stable physical network link. If no Ethernet connection is available, the system falls back to (2) a mobile network connection. As a third alternative, (3) a WiFi connection can be established in WiFi client mode using the internal cellular modem. In this configuration, the radar connects to the WiFi signal broadcast by a nearby access point or by another adjacent radar. The radar units are often deployed in pairs, with each device broadcasting its own WiFi network by default, allowing one radar to operate in client mode and connect to the other. However, this arrangement cannot operate bidirectionally, and the subnets of both cellular modems must be different to avoid conflicts.

Interrupted network connection periods do not prevent new measurements from being recorded. Data are continuously stored locally in a separate folder on the radar's 240 GB SSD. Once the network is restored, all accumulated data are transmitted to the central server and also stored in a backup folder. If an InfluxDB transmission fails, the next measurement trigger will try to resend the previous sweep. This approach prevents packet loss, even if the network connection is interrupted for several hours or days.

Management and debugging of the radar can be performed remotely in two ways. First, the Raspberry Pis are connected to a Tailscale network. By connecting the computer to the same Tailscale network, SSH access to the Raspberry Pis becomes possible. The second option is to use the *Teltonika Remote Management System*, which allows the creation of secure tunnels

to specific ports on the LAN of each radar. For both methods, a stable WAN connection is obviously required. In cases where remote access is impossible due to an interrupted network connection, on-site access may be required. Two approaches can be employed: the first involves creating a hotspot with a specific SSID, to which the Raspberry Pi is configured to connect by default, while the second entails connecting the PC to the WiFi network provided by the cellular modem. Both approaches allow secure access to the Raspberry Pi.

8. Calibration and Preliminary Results

This section presents selected measurement results obtained with the C-band radar systems. As noted earlier in Section 4, calibration measurements are required. To address this, the far-field full-wave radar equation is derived for the proposed radar design. In addition, a field experiment is performed to evaluate and demonstrate the radar's sensitivity. In the remainder of the section, both the time-domain response and Green's function are used. The time-domain response refers to the radar signal observed over time at the receiver, while Green's function represents the theoretical impulse response of the system. Throughout this section, these terms are employed consistently according to their respective context.

8.1. Experimental Verification of the Range Resolution

This first experiment determines the FWHM of the reflected pulse for a radar positioned approximately 2 m from a PEC plate. The resulting pulse is shown in Figure 9. In this measurement, the pulse width is primarily determined by the 2 GHz bandwidth of the SFCW radar. The measured pulse width of 0.612 ns is in good agreement with the theoretically expected value of 0.5 ns, as given by Equation (3). Furthermore, this result confirms that the achieved range resolution of 9.17 cm is consistent with the specifications defined in Section 2.

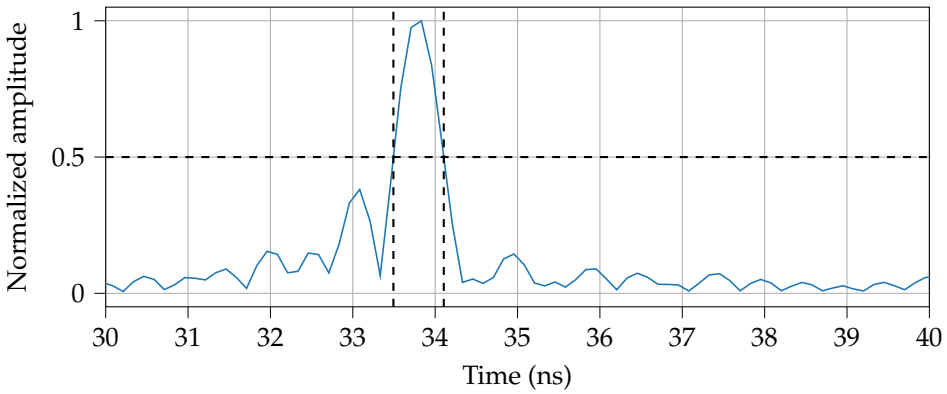

Figure 9. Impulse response of a C-band radar positioned 2 m in front of a PEC plate. The dashed lines indicates how the FWHM was calculated.

8.2. Far-Field Full-Wave Radar Equation

All radar systems were calibrated using the far-field full-wave radar equation developed by Lambot et al. [26]. This formulation explicitly accounts for the radar system, radar–medium interactions and three-dimensional electromagnetic wave propagation in planar, multilayered media through the exact Green's function. The Green's function represents the exact solution of Maxwell's equations describing the electromagnetic field radiated by a unit point source in a given environment [46]. The spatial-domain Green's function is computed as follows:

$$G_{xx} = \frac{1}{8\pi} \int_0^{+\infty} \tilde{G}_{xx}(k_\rho)\, k_\rho \, \mathrm{d}k_\rho, \tag{9}$$

where $\tilde{G}xx(k_\rho)$ is the spectral representation of the Green's function obtained by a Fourier transform with respect to the x and y coordinates, computed by

$$\tilde{G}_{xx}(k_\rho) = \left[J_0(k_\rho \rho) \left(\frac{\Gamma_1 R_1^{\mathrm{TM}}}{\sigma_1 + j\omega\varepsilon_1} - \frac{j\omega\mu_1 R_1^{\mathrm{TE}}}{\Gamma_1} \right) - J_2(k_\rho \rho) \cos(2\theta) \left(\frac{\Gamma_1 R_1^{\mathrm{TM}}}{\sigma_1 + j\omega\varepsilon_1} + \frac{j\omega\mu_1 R_1^{\mathrm{TE}}}{\Gamma_1} \right) \right] \exp(-2\Gamma_1 h_1). \tag{10}$$

where J_0 and J_2 are, respectively, the zero-order and second-order Bessel functions of the first kind; ρ and θ denote the distance and angle in the x–y plane between the field and source points; k_ρ is the spectral-domain counterpart of ρ; subscript 1 refers to the upper half-space; $j = \sqrt{-1}$; R_1^{TM} and R_1^{TE} are, respectively, the transverse magnetic (TM) and transverse electric (TE) global reflection coefficients accounting for all reflections in the multilayered medium; and Γ_1 is the vertical wavenumber defined as $\Gamma = \sqrt{k_\rho^2 - k^2}$, with $k^2 = \omega^2\mu(\varepsilon - j\sigma/\omega)$, where μ is the magnetic permeability, ε the dielectric permittivity, and σ the electrical conductivity. The purpose of the calibration is to remove the intrinsic electromagnetic response of the radar system, including electronics, antennas, transmit–receive antenna coupling and antenna–medium interactions, from the raw frequency-domain measurements. After calibration, the data depend solely on the properties of the observed medium, making the retrieval of the targeted ECVs more robust and physically interpretable. Although the tower-based system uses a bistatic (two-port) VNA configuration, the far-field radar equation can be written in its monostatic form without loss of generality [47,48], provided that the antenna–medium distance is much larger than the transmit–receive aperture. In this regime, the transmit and receive antennas share the same effective phase center, i.e., the same source and field point.

In a bistatic two-port VNA measurement, the recorded quantity is the complex transmission coefficient $S_{21}(\omega)$, representing the global transmission of the emitted field from port 1 through the antenna system, its interaction with the medium and its reception at port 2. Under far-field conditions, the frequency-domain full-wave radar equation is given by

$$S_{21}(\omega) = T_0(\omega) + \frac{T(\omega)\, G_{xx}(\omega)}{1 - G_{xx}(\omega)\, R_s(\omega)}, \tag{11}$$

where

- $T_0(\omega)$: global transmission coefficient of the antenna system from port 1 to port 2 in free-space conditions (intrinsic antenna response);
- $T(\omega) = T_i(\omega)\, T_s(\omega)$, with $T_i(\omega)$ being the global transmission coefficient from port 1 to the effective phase-center source point (transmitting gain) and $T_s(\omega)$ the global transmission coefficient from the effective phase-center field point to port 2 (receiving gain) (only the product $T(\omega)$ is identifiable);
- $R_s(\omega)$: global reflection coefficient for fields incident from the medium toward the radar system, describing the fraction of the backscattered wave reflected again toward the medium;
- $G_{xx}(\omega)$: exact Green's function describing the x-directed backscattered electric field at the antenna phase center for a unit-strength x-directed source at the same point in planar multilayered media.

In free-space conditions, $G_{xx}(\omega) = 0$, and (11) reduces to

$$S_{21}(\omega) = T_0(\omega),$$

meaning that a free-space measurement directly yields the intrinsic global transmission response of the antenna system. This also highlights the importance of minimizing antenna coupling; the weaker the mutual coupling between the transmitting and receiving paths, the more closely the system response approaches ideal behavior and the higher the signal-to-noise ratio. Figure 10 illustrates the physical meaning of the characteristic global reflection and transmission functions. The figure is organized into three layers: the geometric layer, representing the VNA, the RF front end, the free-space region with the antennas and the propagation medium; the second layer, which is the electromagnetic model layer, illustrated by the blue arrows and linked to the functions T_s, T_i, T_0, R_s and G_{xx}; and the third layer, which indicates the physical interpretation of these functions and is highlighted by the green arrows.

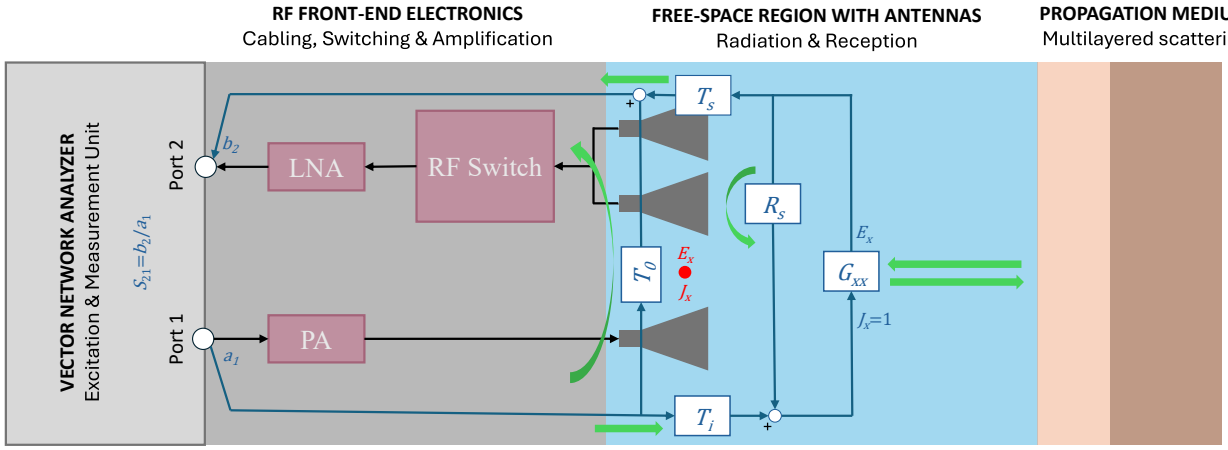

Figure 10. Diagram of the bistatic radar system and the associated global antenna characteristic functions (T_s, T_i, T_0, R_s) used in the far-field full-wave radar equation.

Once the three independent global antenna characteristic functions $T_0(\omega)$, $T(\omega)$ and $R_s(\omega)$ have been identified, the Green's function $G_{xx}(\omega)$ describing the radar–medium interaction can be retrieved directly from the measured VNA transfer function $S_{21}(\omega)$ by inverting Equation (11). The inverted form of the equation is

$$G_{xx}(\omega) = \frac{S_{21}(\omega) - T_0(\omega)}{T(\omega) + S_{21}(\omega)\, R_s(\omega) - T_0(\omega)\, R_s(\omega)}. \tag{12}$$

This inversion removes the intrinsic radar response from the raw measurement and yields a quantity that depends solely on the electromagnetic properties of the observed medium. The retrieved Green's function therefore forms the basis for the quantitative estimation of the targeted ECVs.

The global antenna characteristic functions are identified through a series of laboratory calibration measurements performed under controlled conditions. These measurements are typically acquired at several known distances from a PEC, for which the Green's function $G_{xx}(\omega)$ can be computed. Substituting these known PEC Green's functions into Equation (11) forms a linear system of equations (after rearranging the radar equation) with the three unknown antenna functions $T_0(\omega)$, $T(\omega)$ and $R_s(\omega)$. A minimum of three independent PEC measurements is therefore required to uniquely solve for these three global antenna characteristic functions. In practice, four or five PEC distances are typically used to ensure a well-conditioned characterization problem over the full radar bandwidth [49].

Figure 11 compares the amplitude of the computed Green's function with the raw and calibrated radar measurements for a C-band radar positioned 1.5 m from a PEC. It can be observed that, after calibration, the radar measurements closely match the calculated Green's function. The discrepancy observed between the calculated Green's function and

the calibrated radar measurements after approximately 20 ns is attributed to noise amplification resulting from the application of the dB scale, which is necessary for comparison with the amplitude of the uncalibrated measurements. For the uncalibrated measurements $s_{21}(t)$, the first peak at 17.41 ns corresponds to the coupling, while the second peak at 27.36 ns corresponds to the PEC. The subsequent peaks correspond to the multiple reflections occurring within the radar. After calibration $s_{21,cal}(t)$, the coupling effect is successfully removed, and the first peak at 12.44 ns corresponds to the PEC.

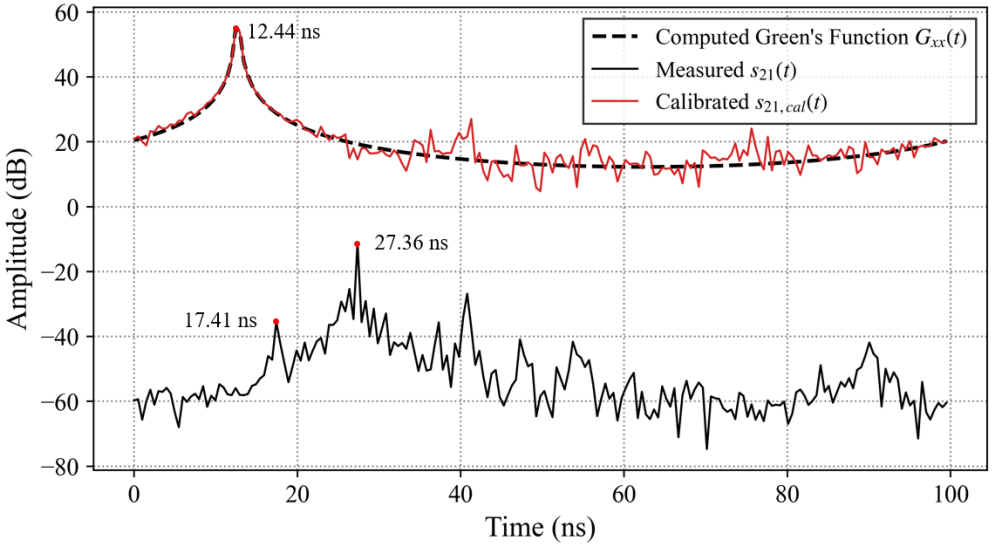

Figure 11. Time-domain amplitude comparison between the measured raw data $s_{21}(t)$, the calibrated measurement $s_{21,cal}(t)$ and the computed Green's function $G_{xx}(t)$ for a C-band radar positioned 1.5 m from a PEC.

Figure 12 shows the raw C-band calibration measurements in the time domain. As expected, reflections from measurements taken at increasing distances from the PEC appear at correspondingly increasing arrival times. The direct coupling term $T_0(\omega)$ is not visible here, as its amplitude is negligible compared to the strong reflection produced by the metal plate. However, this direct coupling is clearly visible in field conditions, as illustrated in Figure 16. For the PEC measurements, multiple reflections at larger times are clearly observable. These arise from (i) internal reflections within the antenna and RF circuitry caused by inherent impedance variations and (ii) multiple two-way interactions between the radar system and the PEC target. In this representation, time zero corresponds to the initial emission instant at the VNA reference plane. After estimating the global antenna characteristic functions, the inversion Equation (12) is applied to the frequency-domain measurements to retrieve the Green's function $G_{xx}(\omega)$, whose time-domain representation is shown in Figure 13. The calibration process successfully removes the intrinsic radar response, including direct coupling and internal multiple reflections, leaving only the single reflection from the PEC. In this calibrated formulation, time zero now corresponds to the effective antenna phase center. Although the phase center of an antenna is theoretically frequency dependent, under far-field conditions and using Equation (11), it can be considered frequency independent and fixed relative to the antenna geometry [50]. Additionally, the XPD is assessed with the radar facing the PEC. An XPD greater than 30 dB is obtained, meaning that the cross-polarized signal is suppressed by more than three orders of magnitude relative to the co-polarized return. The complete set of calibration results, as well as the application of the calibration procedure to field measurements, will be presented in future work.

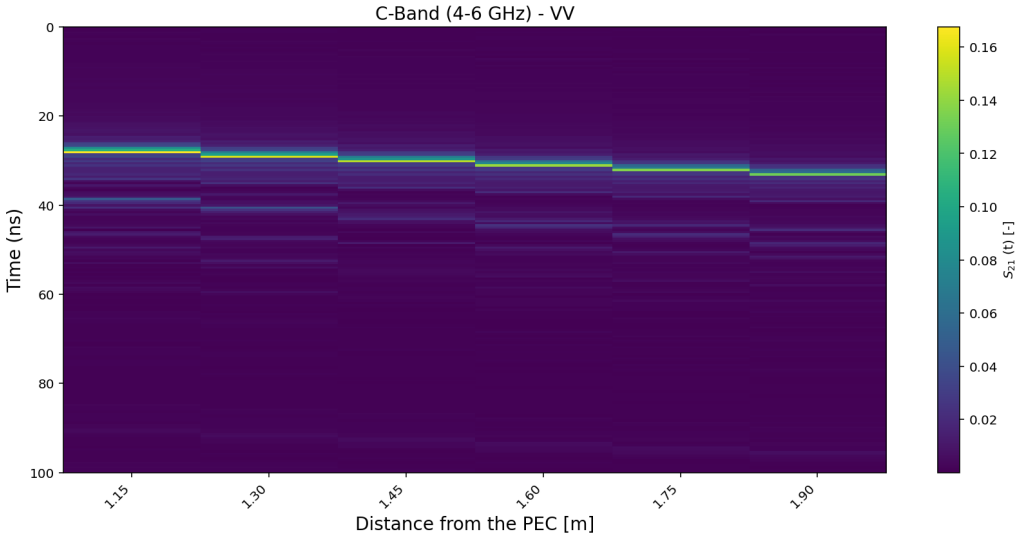

Figure 12. Raw C-band calibration measurements acquired at several distances from a PEC, shown in the time domain as $s_{21}(t)$, i.e., the inverse Fourier transform of $S_{21}(\omega)$.

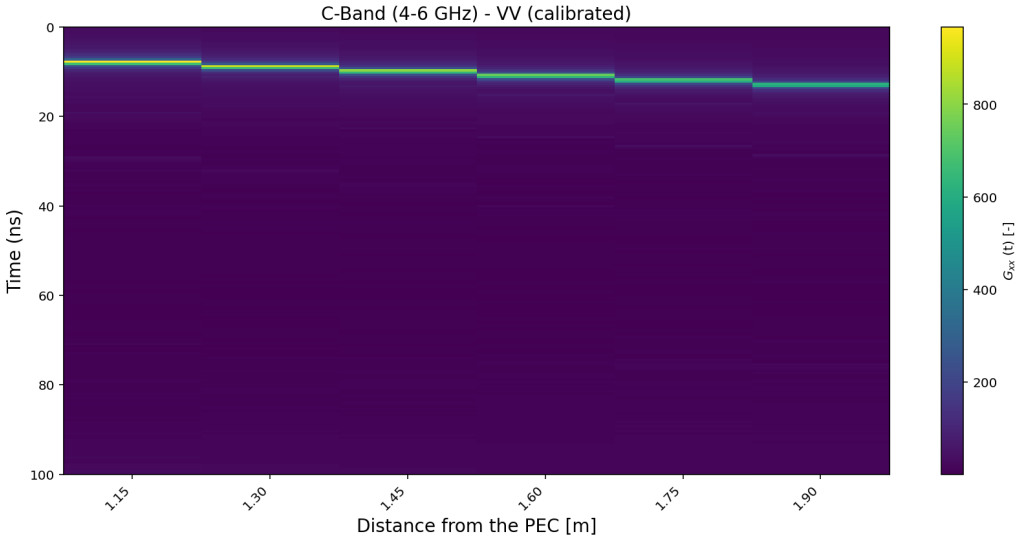

Figure 13. Calibrated C-band PEC measurements acquired at several distances, shown in the time domain as the retrieved Green's function $g_{xx}(t)$ (IFFT of $G_{xx}(\omega)$), obtained after applying the inversion in Equation (12).

8.3. Field Experiments to Validate Radar Sensitivity

To verify the correct functioning of the radar system and to illustrate its sensitivity to nearby targets, a series of controlled shovel-detection experiments was carried out in the C-band at a test site in Switzerland, i.e., Weissfluhjoch. These experiments provide a first-order validation of the radar installation geometry and of the expected range–amplitude response. Figure 14 illustrates the measurement concept. The radar is mounted on a tower and installed at an incidence angle of approximately $\alpha \simeq 40°$, directed towards the ground. A metallic test target, here, the head of a standard steel shovel, is placed at known distances along the illuminated footprint, where 0 m denotes the nadir position directly below the radar. The stepped-frequency radar sweeps across a bandwidth of about 2 GHz for the C-band system. The measured frequency-domain data are transformed to the time domain using an inverse Fourier transform, after which the time axis is converted to a range using the speed of light. Figure 15 shows how this concept is implemented in the field. Only the VV polarization is used in this test. Because the shovel is a compact metallic object

with a smooth surface, it reflects most of the incident VV polarization and produces little depolarization, resulting in a negligible VH response.

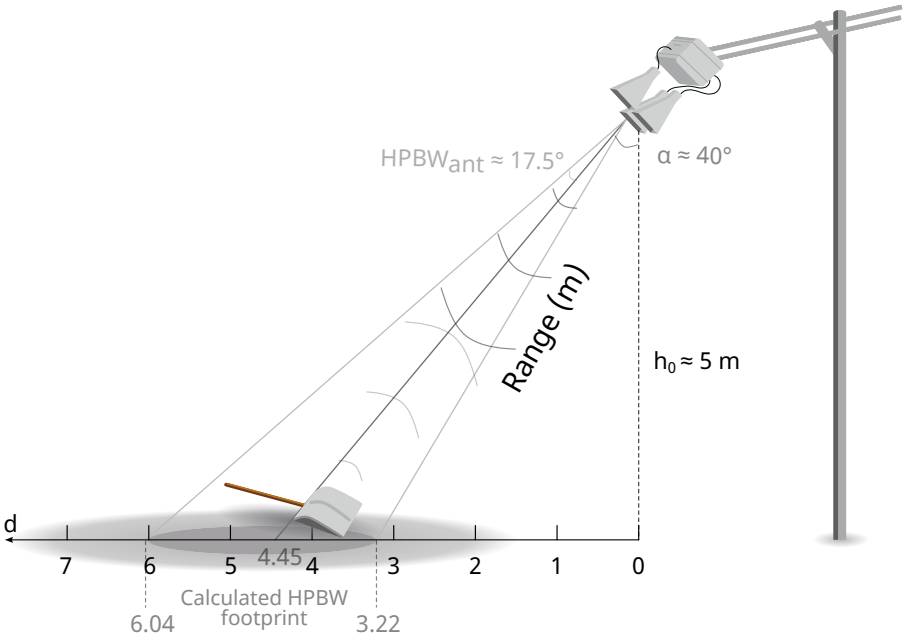

Figure 14. Conceptual illustration of the shovel-detection experiment with the calculated HPBW footprint.

Figure 15. Field setup of the shovel-detection test.

Figure 16 shows the resulting range–amplitude profile for the C-band radar (without calibration). The presented (voltage) amplitude is given as a relative measure and does not depend on the VNA's absolute output power, although the output power of the VNA is set to the maximum (0 dBm) to avoid the reflected signal falling below the noise floor. Three types of measurements are displayed: (i) open-sky measurements without ground in the

main beam, (ii) shovel tests with the target placed at distances between 0 and 10 m and (iii) measurements over soil without the shovel present. The open-sky case mainly reveals a weak residual signal due to antenna coupling and internal reflections. This behavior defines the effective noise floor of the uncalibrated system and can be further reduced when applying the calibration procedure discussed in Section 8.2. When the shovel is present, the radar clearly shows localized increases in backscatter at the corresponding ranges. The strongest reflection is observed when the shovel is placed between about 4 and 5 m from the nadir location, which corresponds to the center of the radar footprint. This confirms that the geometric installation and the data processing are consistent.

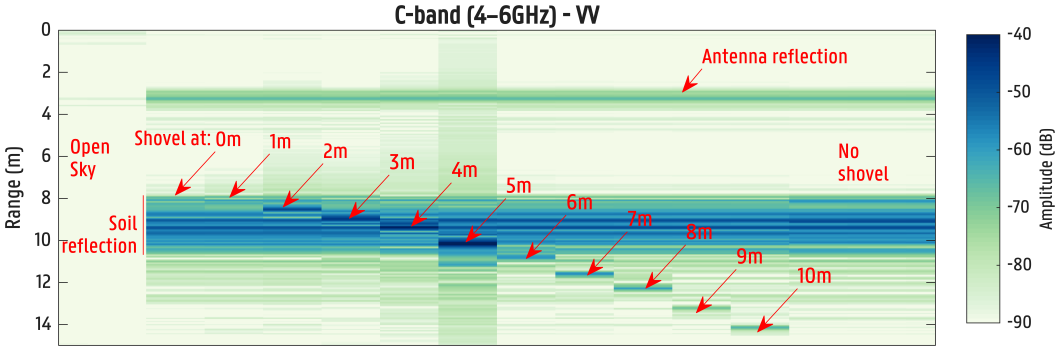

Figure 16. C-band shovel-detection results (4–6 GHz, VV): open-sky measurements, shovel tests at distances 0 to 10 m and soil reflection without the shovel. Object reflections can be clearly observed by analyzing the voltage amplitude. The range axis shows the *uncorrected apparent* slant range ($R = ct/2$), i.e., it includes a constant system delay.

To further validate the geometric consistency of the range processing, the shovel measurements were used to calibrate a simple two-way travel-time model. For a metallic point target located at the ground with a horizontal offset d (measured from nadir), the expected two-way time is

$$t(d) = t_0 + \frac{2}{c}\sqrt{d^2 + h_0^2}, \tag{13}$$

where c is the speed of light, t_0 is an effective constant delay that lumps the RF front end and cable/connector propagation and h_0 is the effective radar height above the ground. The parameters (t_0, h_0) are estimated by nonlinear least-squares fitting using the peak times of the shovel reflections extracted from the VV range–amplitude profiles (Figure 17).

The fit yielded $t_0 = 18.559$ ns and $h_0 = 5.261$ m, with an excellent agreement between observations and model ($R^2 = 0.9983$, RMSE $= 0.56$ ns). Applying the fitted t_0 removed the systematic range bias caused by the uncalibrated internal propagation path; the uncorrected radar-based slant range ($R_{\text{uncorr}} = ct/2$) overestimated the true geometric slant range, while the corrected range ($R_{\text{corr}} = c(t - t_0)/2$) closely matched $R_{\text{geom}} = \sqrt{d^2 + h_0^2}$ for all shovel positions (Table 5). This agreement provides a first-order validation of the installation geometry inferred from the measurements.

Finally, the dominant soil return (marked in Figure 16) can be used as an independent geometric consistency check. Interpreting the time of the maximum soil response at a range distance of 9.431m ($t_{\text{soil}} = 62.917$ ns) as the center of the illuminated footprint on the ground and using Equation (13) yields a horizontal distance $d_{\text{soil}} = 4.07$ m, corresponding to an incidence angle $\alpha = \arctan(d_{\text{soil}}/h_0) = 37.69°$. This is close to the nominal installation angle ($\sim 40°$); remaining differences are likely explained by mechanical tolerances, small mast deflection under load and antenna phase-center uncertainties.

Table 5. Calibration results using shovel reflections. The fitted parameters are $t_0 = 18.559$ ns and $h_0 = 5.261$ m. Correcting for t_0 aligns the radar-derived slant range with the geometric range, providing a first-order validation of the time-to-range conversion and installation geometry.

Shovel Horizontal Distance d [m]	**0**	**1**	**2**	**3**	**4**	**5**	**6**	**7**	**8**	**9**	**10**
Peak time t_{meas} [ns]	52.917	53.917	56.500	59.917	62.417	67.417	72.250	76.917	81.417	87.917	94.333
Model time t_{model} [ns]	53.657	54.285	56.107	58.962	62.649	66.979	71.795	76.977	82.436	88.106	93.941
Residual $t_{\text{meas}} - t_{\text{model}}$ [ns]	−0.740	−0.368	0.393	0.955	−0.232	0.438	0.455	−0.060	−1.019	−0.189	0.392
Geometric slant range $R_{\text{geom}} = \sqrt{d^2 + h_0^2}$ [m]	5.26	5.36	5.63	6.06	6.61	7.26	7.98	8.76	9.57	10.42	11.30
Radar slant range (uncorr.) $R_{\text{uncorr}} = ct/2$ [m]	7.93	8.08	8.47	8.98	9.36	10.11	10.83	11.53	12.21	13.19	14.15
Radar slant range (corr.) $R_{\text{corr}} = c(t - t_0)/2$ [m]	5.15	5.30	5.69	6.20	6.57	7.32	8.05	8.75	9.42	10.40	11.36
Range error $R_{\text{corr}} - R_{\text{geom}}$ [m]	−0.11	−0.06	0.06	0.14	−0.03	0.07	0.07	−0.01	−0.15	−0.03	0.06

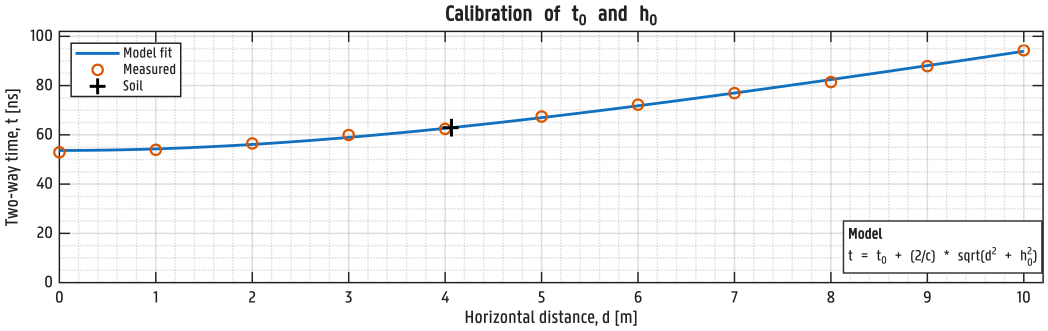

Figure 17. Calibration of the constant system delay t_0 and effective radar height h_0 using the peak two-way times of the shovel reflections extracted from Figure 16. The solid line shows the fitted model, circles denote measured peak times and the plus marker indicates the dominant soil return. The fitted parameters are $t_0 = 18.559$ ns and $h_0 = 5.261$ m ($R^2 = 0.9983$).

Overall, the shovel-detection experiment demonstrates that the radar system responds as expected in terms of geometry, range localization and relative sensitivity, even without advanced calibration, and it provides a useful reference for further scientific analyses.

8.4. Field Experiment with Applied Calibration

As discussed earlier in Section 8.2, the far-field full-wave radar equation aims to isolate the medium response by removing the contributions introduced by the radar system from the measured radar signals. In this way, the resulting measurements depend only on the electromagnetic properties of the investigated medium. This section presents the application of a C-band radar calibration to field data and compares the calibrated measurements with the corresponding uncalibrated data.

In Figure 18, C-band radar measurements acquired over a wheat field with the radar positioned at a height of 5 m and an incidence angle of 40° are shown, both with and without the application of the far-field full-wave radar equation, for the same time window.

It can be observed that, without calibration (a), the coupling effect around 19 ns is so strong that the ground reflection, occurring between 40 and 60 ns, is barely visible. Applying a logarithmic (decibel) transformation would improve the visualization of the data but would not correct the radar-induced effects on the measurements. For the uncalibrated data, the time origin corresponds to the feed point of the VNA.

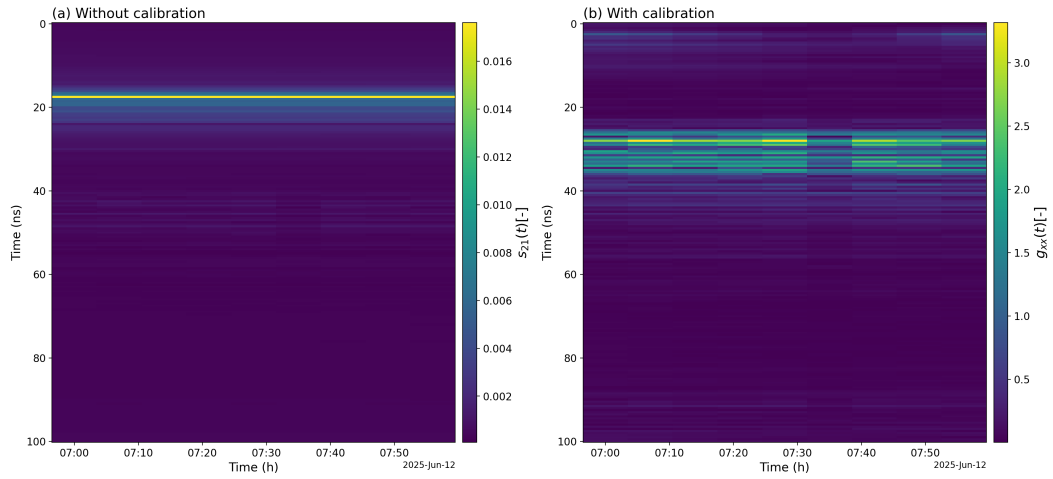

Figure 18. C-band radar measurements performed with the radar attached to a tower (see Figure 2), positioned at 5 m height and tilted at 40°, pointing towards a wheat field. The figure compares measurements over the same 1 h period for (**a**) raw data without calibration, (**b**) data with calibration.

Once the calibration is applied, the ground reflection becomes clearly visible without the need for a decibel transformation. For the calibrated data (b), the time origin corresponds to the virtual source point of the horn antenna, which explains the time shift of the ground reflection, now observed between 20 and 40 ns. However, some residual noise associated with the coupling effect can still be observed in the calibrated measurements. This is attributed to the fact that the current calibration is not yet temperature dependent, although temperature variations are known to affect the radar measurements. A temperature-dependent far-field full-wave radar equation is therefore left for future work, as discussed in the following section. Figure 18 illustrates how the far-field full-wave radar equation successfully removes the noise introduced by the radar system from the field measurements.

9. Future Work

Calibrations using the far-field full-wave radar equation for the proposed radar systems will be presented in detail in a forthcoming publication, together with their application to field measurements, to evaluate the impact of full-wave calibration on the retrieval of ECVs. Particular attention will also be given to temperature-dependent calibration. To quantify temperature-induced drifts under controlled conditions, dedicated calibration experiments will be conducted in a cold-room environment across a representative temperature range ($-35\,^{\circ}$C to $5\,^{\circ}$C). These drifts include temperature-dependent influences from frequency drift from crystal oscillators, conductivity in solid-state microwave components and sensor reading shifts. The tests will be complemented by in situ monitoring to assess temperature-driven drifts during autonomous operation and to evaluate the transferability of laboratory-derived corrections to field conditions. For this purpose, the VNA temperature is already monitored to enable later compensation of the measurement results with known mitigation algorithms (e.g., bin-specific trend compensation or optimal baseline selection). Furthermore, system-level RF characteristics, including insertion loss, polarization isolation and calibration consistency for both polarizations, could be investigated in detail. Here, calibration consistency will be quantified through repeated-sweep stability tests over a static scene and reporting the standard deviation of amplitude and phase in selected range bins and the drift of key reflectors. Their impact on long-term measurement stability and polarimetric performance can be evaluated, particularly in the context of autonomous operation under varying environmental and temperature conditions. Future work will also exploit the full potential of this unique dataset by performing time-series analyses of the backscatter properties, including range profiles, amplitude and phase variations. Beyond sensor and calibration aspects, the dataset also enables process-oriented applications. Examples include snow stability diagnostics (e.g., changes in stratigraphy and wetting/freezing episodes), characterization of infiltration and meltwater percolation dynamics and retrieval or modeling of vegetation water content and its temporal evolution. These ground-based radar observations will be systematically compared with processed Sentinel-1 backscatter signals and in situ measurements of soil, vegetation and snow variables. Physical electromagnetic and radiative-transfer models together with machine learning techniques will be used to better understand the signatures observed by these radar systems and to improve the physical interpretation and retrieval algorithms for satellite products.

10. Conclusions

In this study, a radar system was developed that meets the application requirements for measuring microwave responses from soil and vegetation, as well as the vertical scatter profiles of vegetation–soil and snow–soil. This radar has a new architecture, built around a low-cost, SDR-based VNA, capable of long-term autonomous operation, dual-

band measurements and cloud-based measurement data flow. Both co-polarization and cross-polarization responses can be measured within a compact footprint and across the designated C-band and L-band frequency ranges. A robust and flexible framework has been implemented, enabling continuous monitoring of each individual radar system and allowing remote software updates while also facilitating the replacement or upgrading of antennas and other system components. Phase-center variability, RF coupling, temperature-driven drift and long-term mechanical stability are recognized limitations of the system. Phase-center variability and RF coupling effects are largely mitigated through calibration. Temperature-dependent effects are the subject of ongoing investigation and will be addressed in future work, while long-term mechanical deformations are minimized through a robust mechanical design. Preliminary results indicate that the signal-to-noise ratio is sufficiently high for the intended applications. As the system is now operational and data collection is ongoing, further results will be reported in future work. Once these results become available, the system specifications can be refined and optimized in a subsequent update.

Author Contributions: Conceptualization, J.V.M., B.C., L.D.S., H.L. and S.L.; methodology, J.V.M., B.C., L.D.S., H.L., J.V. and S.L.; software, J.V.M., J.V. and M.M.; validation, J.V.M., J.V., M.M., S.L. and E.T.; formal analysis, L.D.S. and B.C.; investigation, J.V.M. and B.C.; resources, L.D.S., H.L., H.-P.M. and S.L.; data curation, J.V.M.; writing—original draft preparation, J.V.M., B.C., J.V., M.M., S.L. and L.D.S.; writing—review and editing, J.V.M., B.C., L.D.S., H.L., E.T., S.L. and H.-P.M.; visualization, J.V.M., B.C., J.V., M.M. and S.L.; supervision, L.D.S., H.L., H.-P.M. and S.L.; project administration, L.D.S., B.C., H.L., H.-P.M. and S.L.; funding acquisition, B.C., L.D.S., H.L., H.-P.M. and S.L. All authors have read and agreed to the published version of the manuscript.

Funding: This research was supported by the WAVETRAX project, funded by the Belgian Science Policy Office (BELSPO) under grant agreement contract no. SR/00/416.

Data Availability Statement: The original scripts running on the radars to generate the data presented in this study are openly available in the repository *Radar-LibreVNA-Firmware-Zenodo* at [45].

Acknowledgments: The authors thank Guus Leenders for the initial work and contributions that supported the early development of this study. During the preparation of this manuscript, the authors made use of generative AI tools to improve the clarity and quality of the English language. The authors have reviewed and edited the output and take full responsibility for the content of this publication.

Conflicts of Interest: The funders had no role in the design of the study; in the collection, analyses or interpretation of data; in the writing of the manuscript; or in the decision to publish the results. The authors declare no conflicts of interest.

Acronyms and Glossaries

The following acronyms and glossaries are used in this manuscript:

ADC	analog-to-digital converter
COTS	commercial off-the-shelf
CW	continuous wave
DUT	device under test
ECV	essential climate variable
ESA	European Space Agency
FMCW	frequency modulated continuous wave
FPGA	field-programmable gate array
FWHM	full width at half maximum
GPR	ground-penetrating radar
HAT	hardware attached on top
HPBW	half-power beamwidth

IDFT	inverse discrete Fourier transform
IFBW	intermediate frequency bandwidth
LNA	low-noise amplifier
NEOMI	new earth observation mission idea
PA	power amplifier
PEC	perfect electric conductor
PSU	power supply unit
RF	radio frequency
RTC	real time clock
SAR	synthetic aperture radar
SDR	software-defined radio
SFCW	stepped frequency continuous wave
SLAINTE	sub-daily land atmosphere interactions
SNR	signal-to-noise ratio
SRI	stepped repetition interval
SSD	solid state drive
VNA	vector network analyzer
WAN	wide area network
XPD	cross-polar discrimination

References

1. Wagner, W.; Lemoine, G.; Rott, H. A Method for Estimating Soil Moisture from ERS Scatterometer and Soil Data. *Remote Sens. Environ.* **1999**, *70*, 191–207. [CrossRef]
2. Steele-Dunne, S.C.; McNairn, H.; Monsivais-Huertero, A.; Judge, J.; Liu, P.W.; Papathanassiou, K. Radar Remote Sensing of Agricultural Canopies: A Review. *IEEE J. Sel. Top. Appl. Earth Obs. Remote Sens.* **2017**, *10*, 2249–2273. [CrossRef]
3. Tsang, L.; Durand, M.; Derksen, C.; Barros, A.P.; Kang, D.H.; Lievens, H.; Marshall, H.P.; Zhu, J.; Johnson, J.; King, J.; et al. Review article: Global monitoring of snow water equivalent using high-frequency radar remote sensing. *Cryosphere* **2022**, *16*, 3531–3573. [CrossRef]
4. Brisco, B.; Brown, R.; Koehler, J.; Sofko, G.; McKibben, M. The diurnal pattern of microwave backscattering by wheat. *Remote Sens. Environ.* **1990**, *34*, 37–47. [CrossRef]
5. Vermunt, P.C.; Steele-Dunne, S.C.; Khabbazan, S.; Judge, J.; van de Giesen, N.C. Extrapolating continuous vegetation water content to understand sub-daily backscatter variations. *Hydrol. Earth Syst. Sci.* **2022**, *26*, 1223–1241. [CrossRef]
6. Khabbazan, S.; Steele-Dunne, S.; Vermunt, P.; Judge, J.; Vreugdenhil, M.; Gao, G. The influence of surface canopy water on the relationship between L-band backscatter and biophysical variables in agricultural monitoring. *Remote Sens. Environ.* **2022**, *268*, 112789. [CrossRef]
7. Jadoon, K.Z.; Weihermüller, L.; McCabe, M.F.; Moghadas, D.; Vereecken, H.; Lambot, S. Temporal monitoring of the soil freeze-thaw cycles over a snow-covered surface by using air-launched ground-penetrating radar. *Remote Sens.* **2015**, *7*, 12041–12056. [CrossRef]
8. Jadoon, K.Z.; Weihermuller, L.; Scharnagl, B.; Kowalsky, M.B.; Bechtold, M.; Hubbard, S.S.; Vereecken, H.; Lambot, S. Estimation of Soil Hydraulic Parameters in the Field by Integrated Hydrogeophysical Inversion of Time-Lapse Ground-Penetrating Radar Data. *Vadose Zone J.* **2012**, *11*, vzj2011.0177. [CrossRef]
9. Steele-Dunne, S.; Basto, A.; de Zan, F.; Dorigo, W.; Lhermitte, S.; Massari, C.; Matar, J.; Milodowski, D.; Miralle, D.; Monteith, A.; et al. SLAINTE: A SAR mission concept for sub-daily microwave remote sensing of vegetation. In Proceedings of the EUSAR 2024, 15th European Conference on Synthetic Aperture Radar, Munich, Germany, 23–26 April 2024; pp. 870–872.
10. Matar, J.; Sanjuan-Ferrer, M.J.; Rodriguez-Cassola, M.; Steele-Dunne, S.; De Zan, F. A Concept for an Interferometric SAR Mission with Sub-daily Revisit. In Proceedings of the EUSAR 2024, 15th European Conference on Synthetic Aperture Radar, Munich, Germany, 23–26 April 2024; pp. 18–22.
11. Wu, K.; Artois, J.; Tourneur, D.; Mareschal, M.; Henrion, M.; Pathirana, S.; Galagedara, L.; Limbourg, Q.; Lambot, S. Automated drone-borne GPR mapping of root-zone soil moisture for precision irrigation. *Remote Sens. Environ.* **2026**, *333*, 115110. [CrossRef]
12. Henrion, M.; Li, Y.; Wu, K.; Jonard, F.; Opfergelt, S.; Vanacker, V.; Van Oost, K.; Lambot, S. Drone-borne Ground-penetrating radar reveals spatiotemporal moisture dynamics in peatland root zones. *Sci. Remote. Sens.* **2025**, *12*, 100311. [CrossRef]
13. Werner, C.; Wiesmann, A.; Strozzi, T.; Schneebeli, M.; Mätzler, C. The snowscat ground-based polarimetric scatterometer: Calibration and initial measurements from Davos Switzerland. In Proceedings of the 2010 IEEE International Geoscience and Remote Sensing Symposium, Honolulu, HI, USA, 25–30 July 2010; pp. 2363–2366. [CrossRef]

14. Gromek, A. High resolution SAR imaging trials using a handheld vector network analyzer. In Proceedings of the 2014 15th International Radar Symposium (IRS), Gdańsk, Poland, 16–18 June 2014; pp. 1–4. [CrossRef]
15. Leinss, S.; Wiesmann, A.; Lemmetyinen, J.; Hajnsek, I. Snow Water Equivalent of Dry Snow Measured by Differential Interferometry. *IEEE J. Sel. Top. Appl. Earth Obs. Remote Sens.* **2015**, *8*, 3773–3790. [CrossRef]
16. Chen, X.; Siqueira, P. A ground-based L-band synthetic aperture radar system for forest temporal dynamics monitoring. In Proceedings of the 2017 IEEE International Geoscience and Remote Sensing Symposium (IGARSS), Fort Worth, TX, USA, 23–28 July 2017; pp. 3429–3432. [CrossRef]
17. Brangers, I.; Marshall, H.P.; De Lannoy, G.; Dunmire, D.; Mätzler, C.; Lievens, H. Tower-based C-band radar measurements of an alpine snowpack. *Cryosphere* **2024**, *18*, 3177–3193. [CrossRef]
18. Albinet, C.; Borderies, P.; Koleck, T.; Rocca, F.; Tebaldini, S.; Villard, L.; Le Toan, T.; Hamadi, A.; Ho Tong Minh, D. TropiSCAT: A Ground Based Polarimetric Scatterometer Experiment in Tropical Forests. *IEEE J. Sel. Top. Appl. Earth Obs. Remote Sens.* **2012**, *5*, 1060–1066. [CrossRef]
19. El Idrissi Essebtey, S.; Villard, L.; Borderies, P.; Koleck, T.; Monvoisin, J.P.; Burban, B.; Le Toan, T. Temporal Decorrelation of Tropical Dense Forest at C-Band: First Insights From the TropiScat-2 Experiment. *IEEE Geosci. Remote Sens. Lett.* **2020**, *17*, 928–932. [CrossRef]
20. Ulander, L.M.H.; Monteith, A.R.; Soja, M.J.; Eriksson, L.E.B. Multiport Vector Network Analyzer Radar for Tomographic Forest Scattering Measurements. *IEEE Geosci. Remote Sens. Lett.* **2018**, *15*, 1897–1901. [CrossRef]
21. Ulander, L.M.H.; Monteith, A.R.; Persson, H.J.; Fransson, J.E.S. Borealscat-2: Backscatter Measurements of Forest Water Dynamics. In Proceedings of the IGARSS 2024—2024 IEEE International Geoscience and Remote Sensing Symposium, Athens, Greece, 7–12 July 2024; pp. 2332–2335. [CrossRef]
22. Zhou, Z.S.; Boerner, W.M.; Sato, M. Development of a ground-based polarimetric broadband SAR system for noninvasive ground-truth validation in vegetation monitoring. *IEEE Trans. Geosci. Remote Sens.* **2004**, *42*, 1803–1810. [CrossRef]
23. Wiesmann, A.; Caduff, R.; Werner, C.; Frey, O.; Schneebeli, M.; Löwe, H.; Jaggi, M.; Schwank, M.; Naderpour, R.; Fehr, T. ESA SnowLab Project: 4 Years Of Wide Band Scatterometer Measurements Of Seasonal Snow. In Proceedings of the IGARSS 2019—2019 IEEE International Geoscience and Remote Sensing Symposium, Yokohama, Japan, 28 July–2 August 2019; pp. 5745–5748. [CrossRef]
24. Jorge Ruiz, J.; Vehmas, R.; Lemmetyinen, J.; Uusitalo, J.; Lahtinen, J.; Lehtinen, K.; Kontu, A.; Rautiainen, K.; Tarvainen, R.; Pulliainen, J.; et al. SodSAR: A Tower-Based 1–10 GHz SAR System for Snow, Soil and Vegetation Studies. *Sensors* **2020**, *20*, 6702. [CrossRef]
25. Alonso, R.; García del Pozo, J.M.; Buisán, S.T.; Álvarez, J.A. Snow Water Equivalent Evolution During the 2019/2020 Winter Period in Aemet-Formigal Test Site Using a SFCW Radar. In Proceedings of the 2021 IEEE International Geoscience and Remote Sensing Symposium IGARSS, Virtual, 12–16 July 2021; pp. 1035–1038. [CrossRef]
26. Lambot, S.; Slob, E.; van den Bosch, I.; Stockbroeckx, B.; Vanclooster, M. Modeling of ground-penetrating Radar for accurate characterization of subsurface electric properties. *IEEE Trans. Geosci. Remote Sens.* **2004**, *42*, 2555–2568. [CrossRef]
27. WAVETRAX: Water and Vegetation Tower Radar Experiments for Improved Climate Monitoring. 2025. Available online: https://www.belspo-wavetrax.be/ (accessed on 19 January 2026).
28. Wu, K.; Rodriguez, G.A.; Zajc, M.; Jacquemin, E.; Clément, M.; De Coster, A.; Lambot, S. A new drone-borne GPR for soil moisture mapping. *Remote Sens. Environ.* **2019**, *235*, 111456. [CrossRef]
29. Consulting, S. gprSense®—Precision Subsurface Sensing for Agriculture & Gheophysics. Available online: https://www.gprsense.com/ (accessed on 19 January 2026).
30. Brangers, I.; De Lannoy, G.; Marshall, H.P.; Dunmire, D.; Bonnell, R.; Cox, B.; Cappelle, J.; Brad Baxter, W.; Lievens, H. C-Band Radar Measurements in a Snow-Covered Boreal Forest Environment. *IEEE Geosci. Remote Sens. Lett.* **2025**, *22*, 1–5. [CrossRef]
31. Lievens, H.; Demuzere, M.; Marshall, H.P.; Reichle, R.H.; Brucker, L.; Brangers, I.; de Rosnay, P.; Dumont, M.; Girotto, M.; Immerzeel, W.W.; et al. Snow depth variability in the Northern Hemisphere mountains observed from space. *Nat. Commun.* **2019**, *10*, 4629. [CrossRef]
32. Vreugdenhil, M.; Navacchi, C.; Bauer-Marschallinger, B.; Hahn, S.; Steele-Dunne, S.; Pfeil, I.; Dorigo, W.; Wagner, W. Sentinel-1 cross ratio and vegetation optical depth: A comparison over Europe. *Remote Sens.* **2020**, *12*, 3404. [CrossRef]
33. Krabbe, L.; Haberberger, N.; Stelzig, M.; Pfluger, F.; Braun, M.; Vossiek, M. Design and Verification of a Versatile and Lightweight Radar Platform for High-Resolution Imaging of Glacial Subsurface Structures. *IEEE J. Microwaves* **2024**, *4*, 871–880. .. [CrossRef]
34. Xethru. *X2 Impulse Radar Transceiver*; Technical Report; XeThru: Oslo, Norway, 2015.
35. Nicolaescu, I.; van Genderen, P.; Van Dongen, K.; van Heijenoort, J.; Hakkaart, P. Stepped frequency continuous wave radar-data preprocessing. In Proceedings of the 2nd International Workshop onAdvanced Ground Penetrating Radar, Delft, The Netherlands, 14–16 May 2003; pp. 177–182. [CrossRef]

36. Parrini, F.; Papi, F.; Pieraccini, M. An ultra high resolution stepped frequency GPR for civil engineering applications. In Proceedings of the 2015 8th International Workshop on Advanced Ground Penetrating Radar (IWAGPR), Florence, Italy, 7–10 July 2015; pp. 1–4. [CrossRef]
37. Noon, D.A. Stepped-Frequency Radar Design and Signal Processing Enhances Ground Penetrating Radar Performance. Ph.D. Thesis, The University of Queensland, St. Lucia, Australia, 1996.
38. Seyfried, D.; Schoebel, J. Stepped-frequency radar signal processing. *J. Appl. Geophys.* **2015**, *112*, 42–51. [CrossRef]
39. Jankae. LibreVNA User Manual. Manual, LibreVNA Project, GitHub. 2021. Available online: https://github.com/jankae/LibreVNA/blob/master/Documentation/UserManual/manual.pdf (accessed on 19 January 2026).
40. Pico Technology. *PicoVNA Vector Network Analyzer Data Sheet*; Technical Report; Pico Technology: Cambridgeshire, UK, 2023. Available online: https://www.picotech.com/download/datasheets/picovna-vector-network-analyzer-data-sheet.pdf (accessed on 1 December 2025).
41. Jankae. LibreVNA Specification Sheet. Specsheet, LibreVNA Project, GitHub. 2024. Available online: https://github.com/jankae/LibreVNA/blob/master/Documentation/UserManual/specsheet.pdf (accessed on 19 January 2026).
42. Ali, Z.; Elsayed, M.; Tiwari, G.; Ahmad, M.; Le Kernec, J.; Heidari, H.; Gupta, S. Impact of receiver thermal noise and PLL RMS jitter in radar measurements. *IEEE Trans. Instrum. Meas.* **2024**, *73*, 2002710. [CrossRef]
43. Carey, S.C.; Scott, W.R. Software defined radio for stepped-frequency, ground-penetrating radar. In Proceedings of the 2017 IEEE International Geoscience and Remote Sensing Symposium (IGARSS), Fort Worth, TX, USA, 23–28 July 2017; pp. 4825–4828. [CrossRef]
44. Takahashi, K.; Miwa, T. Near-Range SFCW UWB Radar Based on Low-Cost Software Defined Radio. In Proceedings of the 2019 IEEE Radar Conference (RadarConf), Boston, MA, USA, 22–26 April 2019; pp. 1–6. [CrossRef]
45. Van Mulders, J. Van Mulders, J. *Wavetrax-by-Dramco/Radar-LibreVNA-Firmware-Zenodo*, V0.1.5; CERN: Geneva, Switzerland, 2025. [CrossRef]
46. Chew, W.C. *Waves and Fields in Inhomogeneous Media*; Van Nostrand Reinhold: New York, NY, USA, 1990.
47. Lambot, S.; Andre, F. Full-Wave Modeling of Near-Field Radar Data for Planar Layered Media Reconstruction. *IEEE Trans. Geosci. Remote Sens.* **2014**, *52*, 2295–2303. [CrossRef]
48. Tran, A.P.; Andre, F.; Craeye, C.; Lambot, S. Near-field or far-field full-wave ground penetrating radar modeling as a function of the antenna height above a planar layered medium. *Prog. Electromagn. Res. Pier* **2013**, *141*, 415–430. [CrossRef]
49. Lambot, S.; Antoine, M.; Vanclooster, M.; Slob, E.C. Effect of soil roughness on the inversion of off-ground monostatic GPR signal for noninvasive quantification of soil properties. *Water Resour. Res.* **2006**, *42*, W03403. [CrossRef]
50. Jadoon, K.Z.; Lambot, S.; Slob, E.C.; Vereecken, H. Analysis of Horn Antenna Transfer Functions and Phase-Center Position for Modeling Off-Ground GPR. *IEEE Trans. Geosci. Remote Sens.* **2011**, *49*, 1649–1662. [CrossRef]